Thermal Science and Engineering Progress 18 (2020) 100543

Contents lists available at ScienceDirect

Thermal Science and Engineering Progress

journal homepage: www.elsevier.com/locate/tsep

A review of printed circuit heat exchangers for helium and supercritical CO_2 Brayton cycles

Lei Chai*, Savvas A. Tassou

Centre for Sustainable Energy Use in Food Chain (CSEF), Institute of Energy Futures, Brunel University London, Uxbridge, Middlesex UB8 3PH, UK

ARTICLE INFO

Keywords:
Printed circuit heat exchangers
Heat transfer
Pressure drop
Design optimisation
Helium and supercritical CO_2 Brayton cycles

ABSTRACT

Printed circuit heat exchangers (PCHEs) are a promising technology for helium and supercritical CO_2 Brayton cycles due to their highly compact construction, very high heat transfer coefficients, capability to withstand high pressures and wide range of operating temperatures. The purpose of this review is to provide a comprehensive understanding of the performance of PCHEs based on available literature and survey of heat exchangers currently available on the market. First, the fundamental principles, including material selection, manufacturing and assembly, are introduced. Then, PCHEs with different flow passages are summarized and analysed along with their heat transfer and pressure drop characteristics. Next, geometric design optimisation of PCHEs is summarised and discussed, taking into consideration the complex relationships between heat transfer enhancement and pressure drop penalty, compactness and fluid inventory as well as capital cost. Finally, knowledge gaps are identified and suggestions for further research to address these for a wider range of applications are presented. The review covers relatively new heat exchangers on the market as well as designs that are still under development. Although extensive work has already been done in this field, and PCHEs are well established in the petrochemical industry, significantly more work is needed to increase their attractiveness for a wider range of applications. This work should be aimed at the optimisation of flow passage configurations in terms of thermohydraulic performance, complexity and manufacturing costs, development and selection of materials to increase further the range of high temperature and pressure operation, and the development of more generalised correlations for performance prediction and overall design optimisation.

1. Introduction

For power generation and heat to power conversion systems, advanced nuclear reactors have attracted the attention of various scholars in the field of future energy technologies, due to the global increase in electrical energy demand, environmental concerns, economic benefits and the multi-purpose potential application of this technology [1]. A gas-cooled fast reactor scheme from 4th generation nuclear systems is shown in Fig. 1. Its reference value of coolant inlet/outlet temperature and pressure is 490 °C/850 °C and at 90 bar, respectively. This can be achieved through the Rankine cycle with high pressure steam generators, the Brayton cycle with helium gas turbines, or the supercritical CO_2 Brayton cycle [2]. The helium Brayton cycle has been primarily envisioned for electricity production and actinide management due to its closed fuel cycle and excellent actinide management capability. Since helium typically has a low heat transfer capability due to its low volumetric thermal capacity and low thermal conductivity, a compact heat exchanger with a high surface-area-to-volume ratio is advantageous for thermal energy transfer [3,4]. Due to its potential for high electricity generation efficiency, the supercritical CO_2 Brayton cycle, has also attracted significant attention in recent years for high temperature heat to power conversion applications [5,6]. A supercritical CO_2 with low viscosity and high thermal conductivity can result in good compatibility with standard materials, lower compressive work, good tolerance and robustness with the turbine and compressor and good availability for heat sinks and sources due to the relatively low temperature required for maintaining the supercritical condition [7–10]. In such power generation and conversion systems, the efficiency of the electricity generation is critically dependent on heat exchangers, which are key components in transferring the thermal energy, and can be used as the heater, condenser, gas cooler and recuperator. Among the various types of heat exchangers, the printed circuit heat exchanger (PCHE) is a good candidate for heat sourcing and sinking of helium and supercritical CO_2 due to its favourable attributes of high compactness and structural rigidity, high efficiency and effectiveness, and its reliable performance under conditions of extreme pressure and

* Corresponding author.
E-mail address: Lei.Chai@brunel.ac.uk (L. Chai).

https://doi.org/10.1016/j.tsep.2020.100543
Received 29 January 2020; Received in revised form 3 April 2020; Accepted 3 April 2020

Nomenclature

a	parameter
A	heat transfer area, m^2
b	parameter
c	parameter
c_p	specific heat, $J \cdot kg^{-1} K^{-1}$
d	diameter, m; parameter
D	hydraulic diameter, m
Eu	Euler number, $Eu = \frac{2\Delta p}{\rho v^2}$
f	friction factor
g	gravitational acceleration, $m \cdot s^{-2}$; gap
Gr	Grashof number
Gz	Graetz number
G_v	volume-goodness factor
h	heat transfer coefficient, $W \cdot m^{-2} K^{-1}$
j	Colburn factor, $j = \frac{Nu}{RePr^{1/3}}$
k	thermal conductivity, $W \cdot m^{-1} K^{-1}$
l	length, m
$\dot{m}$	mass flow rate, $kg \cdot s^{-1}$
n	number of channels
Nu	Nusselt number, $Nu = \frac{hD}{k}$
p	pressure, Pa; pitch, m
Pr	Prandtl number, $Pr = \frac{\mu c_p}{k}$
Q	heat transfer rate, W
Re	Reynolds number, $Re = \frac{\rho v D}{\mu}$
S	shape factor
S_g	entropy generation rate
T	temperature, K
T_{pc}	critical temperature at operating pressure, K
U	overall heat transfer coefficient, $W \cdot m^{-2} K^{-1}$
v	velocity, $m \cdot s^{-1}$
w	width, m
x	length along the channel, m
Δp	pressure drop, Pa

Greek letters

θ	fin angle
η	performance evaluation criteria
ρ	density, $kg \cdot m^{-3}$
μ	dynamic viscosity, Pa·s
ν	kinematic viscosity, $m^2 \cdot s^{-1}$
τ	shear stress, Pa
ε	heat transfer effectiveness

Subscripts

ave	average
act	actual
c	channel; cold
cal	calculation
exp	experimental
f	fin
h	hot
in	inlet
max	maximum
min	minimum
opt	optimal
pp	pumping power
ref	reference
w	wall

temperature.

PCHE, also known as diffusion-bonded microchannel heat exchanger, or compact platelet heat exchanger, is a promising heat exchanger technology. The concept of the PCHE was originally invented at the University of Sydney in the early 1980s and was commercialised by Heatric in Australia in 1985 [11–13]. For PCHE, the flow passages are manufactured by photochemical machining into a flat plate, with the plates then stacked together and diffusion bonded. This manufacturing process is similar to that used for the manufacture of electronic printed circuit boards, hence the common description as PCHE. Photochemical machining, also known as photochemical milling or photo etching, is one of the least-well-known non-conventional machining processes. It employs chemical etching through a photoresist stencil to remove material over selected areas [14]. Diffusion bonding, also known as diffusion welding, is a solid-state welding technique by which two surfaces are bonded together under high temperature and mechanical pressure in a vacuum or non-oxygen environment wherein the atoms of two solid, metallic surfaces intersperse themselves over time [15]. As a result of these two advanced techniques, PCHEs have a compact and high-integrity core making them suitable for high pressure and high temperature applications. Recently, more manufacturers have also entered the compact heat exchanger market, including HEXCES, VPE and Alfa Laval. Fig. 2 shows a typical PCHE and its diffusion-bonded core.

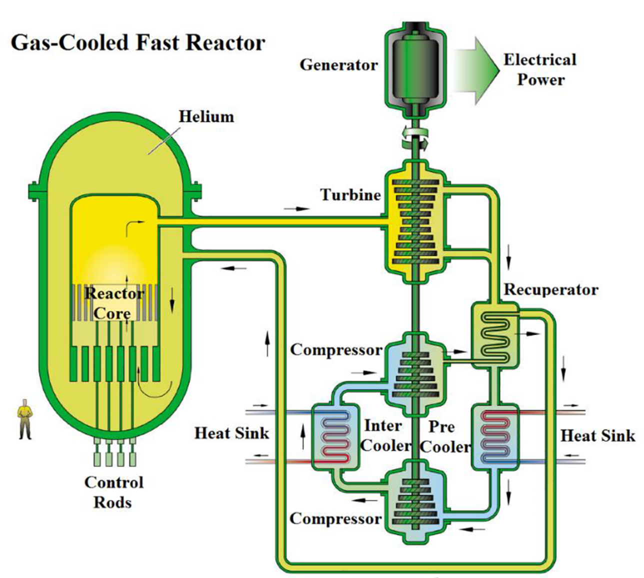

Fig. 1. A gas-cooled fast reactor scheme from 4th generation nuclear systems [1].

In recent years, new frontiers have been opened up for PCHE designs and applications, particularly for supercritical CO_2 and helium Brayton cycles. Several review papers have also been published in this area to present the state of the art. Ahn et al. [17] summarized the various layouts and development status of the supercritical CO_2 power cycle. Cheng et al. [18] and Cabeza et al. [19] reviewed the heat transfer and pressure drop of supercritical CO_2 flowing in channels, but both reviews were based only on results of experimental investigations and heat transfer correlations. Huang et al. [20] summarized the characteristics of flow and heat transfer in PCHEs based on experimental results and simulations but did not discuss material selection, manufacturing and assembly, and heat exchanger optimization methods. Overall, in previous works technical challenges related to the design and operation of PCHEs at high temperature and pressure have not been addressed in detail. PCHEs operating in these conditions require more detailed thermal and mechanical analysis and larger safety

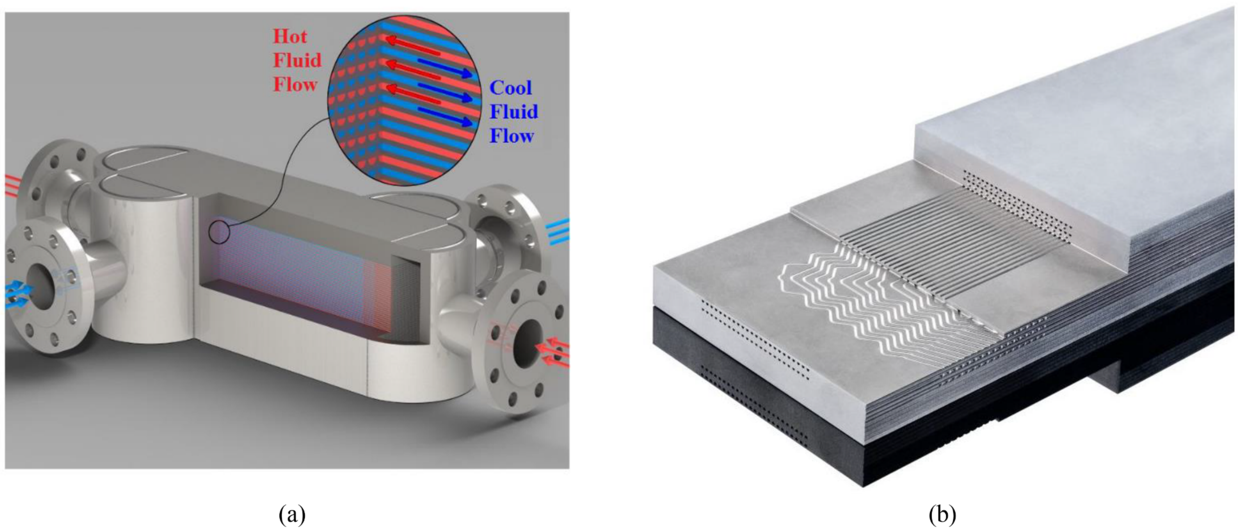

Fig. 2. Typical PCHE (a) Cutaway image and (b) Diffusion-bonded core [16].

margins than conventional heat exchangers [21]. To contribute towards addressing these challenges, this review paper focuses on the fundamental principles of PCHE, including material selection, manufacturing and assembly, thermal and hydraulic performance, and optimization of the geometric design, all with the purpose of providing a comprehensive understanding of PCHEs, design considerations and their performance characteristics. Unlike the work of Huang et al. [20] that reviewed PCHEs by considering separately experimental studies and numerical simulations, the review in this paper considers in significant detail PCHE performance in terms of flow passage geometry and flow characteristics, material selection, manufacturing techniques and design optimisation.

2. Material selection

For helium and supercritical CO_2 cycles, the PCHE must be able to operate at elevated pressures and temperatures, limited by corrosion, oxidation and creep resistance of the selected materials [22]. For PCHE, the pressure and temperature differentials can result in high internal stresses, which can cause significant flow passage deformation leading to eventual failure of the PCHE [23]. Moreover, many current PCHEs employ 316/316L/347 stainless steel, which limits the operating temperature to 600–650 °C due to creep and corrosion limitations [24]. For higher temperatures, PCHEs have to employ nickel-based alloys or titanium at much higher capital cost. Materials for diffusion-bonded PCHEs are summarized in Table 1. The choice depends on the requirements, including service conditions, pressure containment and corrosion, among others. In terms of safety considerations for PCHE applications in helium and supercritical CO_2 Brayton cycles, the research on material selection mainly focuses on thermal stresses and corrosion.

Creep is an important consideration in the design of PCHEs. Permanent creep deformation may occur in the compact flow passages, which can be detrimental on the thermohydraulic performance of the heat exchanger and may cause the compressor discharge gas passages to expand, thereby increasing the turbine backpressure and potentially impacting the safety of the whole system operation [25]. Oak Ridge National Laboratory (ORNL) and ATI Allegheny Ludlum have done much work on improving the performance of alloy materials for compact heat exchangers. Maziasz et al. [26–29] tested the creep resistance of a group of heat-resistant and oxidation/corrosion-resistant austenitic stainless alloys at high temperatures (650–800 °C), covering Type 347 stainless steel and Alloy 120, 214, 230, 625, 740, 803, HR120 and AL20-25 + Nb. The results showed that standard 347 stainless steel cannot be used when the temperature exceeds 650 °C, while alloys such as Alloy 214, 625, HR120 and AL20-25 + Nb can have very good properties for high temperatures, especially with careful control of microstructure during processing. Fig. 3 shows the SEM micrographs of standard 347 stainless steel and Alloy 625 to characterize the microstructural changes and to identify the precipitate phases forming during creep. For standard 347 stainless steel, Fe-Cr σ-phase at the grain boundary triple points formed after only 51.4 h creep at 704 °C, while for Alloy 625, a relatively stable dispersion of Si-Mo-Cr-Ni M6C phase developed and remained stable along the grain boundaries even after 4510 h operation at 750 °C and 100 MPa, indicating that Alloy 625 has significantly better creep resistance than the standard 347 stainless steel at temperatures higher than 700 °C. Osman et al. [30] also found that thin foil specimens of 347 stainless steel had higher creep rates and higher rupture ductility than their bulk specimen counterparts and cannot be used at temperatures above 700 °C. Evans et al. [31] employed both scanning and transmission electron microscopy to correlate microstructures with the creep behaviour of Alloy 625. A short-time heat treatment of the processed foils at 900 °C was shown to produce the typical commercial foil microstructure and creep properties, indicating that Alloy 625 is an attractive potential alloy for use in the production of PCHEs for operation at high temperature. Li et al. [32] compared the maximum allowable stress of different materials such as Alloy 800H, HX, 230 and 617 at a high temperature (900 °C) and suggested that Alloy 617 was the leading candidate material for high temperature heat exchangers. Klöwer et al. [33] also suggested Alloy 617 as a candidate material for 700 °C power plants due to its combination of creep strength and good fabricability. However, Alloy 617 has not yet been approved by the ASME boiler and pressure vessel code

Table 1
Materials for diffusion-bonded PCHE.

Stainless Steel	Nickel	Titanium
Type 304	Alloy 59	CP grade
Type 316 / 316L	Alloy 600	Grade 5
Type 347	Alloy 625	22 Cr duplex
AL-6XN	Alloy 617	
	Alloy 800H	
	Alloy 800HT	
	Alloy 230	
	Alloy 740H	
	Alloy HX	
	Alloy 556	
	Alloy HR-160	

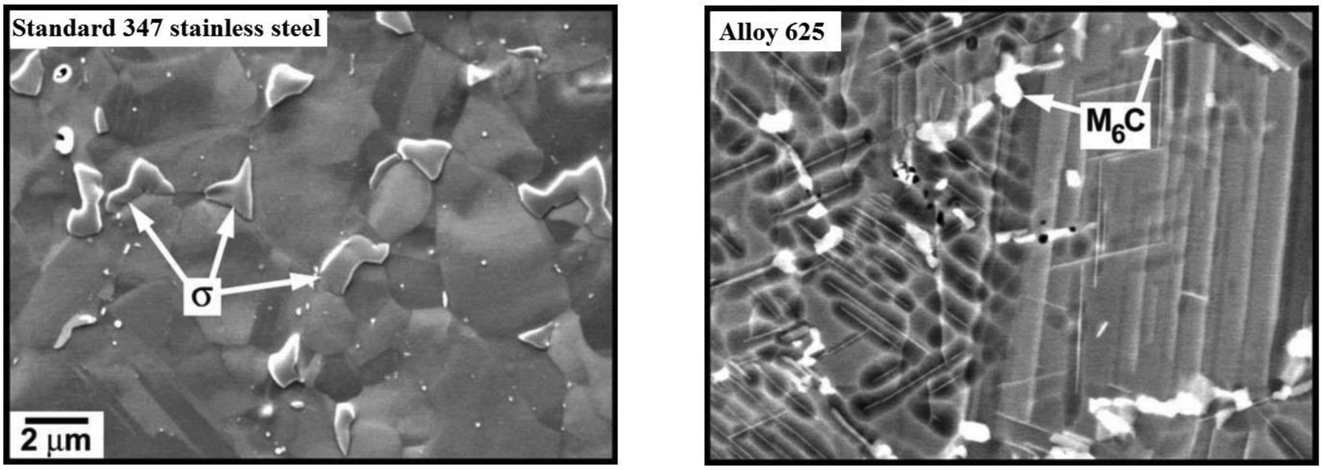

(a) (b)

Fig. 3. SEM micrographs of creep-tested foils for (a) Standard 347 stainless steel and (b) Alloy 625 [29].

[34,35]. Work is on-going to develop a database for the composition refinement, mechanical properties, creep–fatigue, corrosion regimes, and microstructural and mechanical properties of Alloy 617 [36–40].

Corrosion is another important factor in material selection for PCHE, especially for supercritical CO_2 because helium is inert [41]. The previous research has focused on the oxidation performance and corrosion properties of compact heat exchanger materials in water vapour, moist air or exhaust gas. Comprehensive databases, selection rules, and design guidelines for high temperature alloys have been developed for thick-section pressure vessels and piping applications [24,26,27,42,43,44]. However, little research exists into the oxidation performance and corrosion properties at high temperatures for supercritical CO_2. More recently, the University of Wisconsin–Madison, the Korea Advanced Institute of Science and Technology, and the National Energy Technology Laboratory, USA, have focused on research on the corrosion behaviour of alloys in supercritical CO_2 high-temperature environments. Anderson et al. [45,46] designed and constructed a facility for corrosion testing of materials in supercritical CO_2 environments at temperatures and pressures up to 650 °C and 3925 psi, respectively. They first performed corrosion testing on ferritic steels NF616 and HCM12A, austenitic alloys IN 800H and 347 stainless steel, and a range of advanced concept alumina forming austenitic alloys in the temperature range of 450 °C to 650 °C and 3000 psi. Results showed that Cr and Al had profound influence on imparting corrosion resistance under these test conditions. Cao et al. [47] tested the corrosion behaviour of three austenitic alloys, 316SS and 310SS and Alloy 800H in supercritical CO_2 at 650 °C and 20 MPa for 3000 h. Results showed that Alloy 800H exhibited the best corrosion resistance, followed by 310SS and 316SS, and that the oxidation of Alloy 800H and 310SS followed a diffusion-controlled parabolic growth law, while 316SS exhibited a higher oxide growth rate with more pronounced oxide spallation. Firouzdor et al. [48] studied the corrosion of four alloys at 650 °C and 20 MPa up to 3000 h, specifically AL-6XN stainless steel and three nickel-based alloys, PE-16, Haynes 230, and Alloy 625. Results in Fig. 4 which presents a plan view of SEM images of the surface oxide morphology of Alloy 625 samples exposed to supercritical CO_2 for 500 h, 1000 h and 3000 h, show that Cr_2O_3 oxide forms on the surface of the samples after 500 h exposure to high temperature and pressure CO_2 and protects the alloy from further corrosion. Lee et al. [49,50] investigated the corrosion and carburization behaviour of chromia-forming heat-resistant alloys 800HT, 600 and 690, by exposing the alloys to 550 °C, 600 °C and 650 °C at 20 MPa for 1000 h. For all alloys, a thin and continuous Cr_2O_3 layer was formed on the surface, while the existence of an amorphous carbon layer was identified at the chromia/matrix interface. Below the amorphous C-layer, Cr-rich $M_{23}C_6$ carbides were extensively formed in Alloy 800HT but not in Alloy 600 or Alloy 690. Rouillard et al. [51] studied the corrosion behaviour of different structural metallic materials for heat exchangers, typically one ferritic-martensitic steel T91 and several austenitic steels 316L, 253MA® and Alloy 800 under static supercritical CO_2 at 550 °C and 250 bar. Results showed that the austenitic alloys were much more corrosion-resistant than T91. After 310 h, a thin protective Cr-rich oxide layer formed on the austenitic steels, whereas thicker, iron-rich, duplex scale grew on the ferritic-martensitic steel, which could be detrimental for the thermal conductivity of heat exchangers and, thus, the global cycle efficiency. Holcomb et al. [52] compared the oxidation behaviour of austenitic stainless steels and nickel-based alloys in supercritical water (726 °C/208 bar) and supercritical CO_2 (730 °C/207 bar). They found that nickel-based alloys in supercritical CO_2 did not exhibit much change with pressure, while nickel-based alloys in supercritical water had an increase in corrosion rate, with the log of the parabolic rate constant being proportional to pressure. Féron et al. [53] reviewed the corrosion behaviour of metals and alloys in supercritical fluids and concluded that oxidation and carburization in supercritical CO_2 may occur at between 450 °C and 650 °C for alloys. Nickel-based alloys with high chromium content were found to exhibit better corrosion resistance than stainless steel.

3. Manufacturing and assembly

The manufacturing process of PCHE begins with thin sheets of metal that are photochemically etched with specific design patterns before the individual platelets are accurately assembled and joined by a diffusion-bonding process to form a compact, strong, all-metal structure containing complex internal passages that allow for precise flow control, fluid manifolding and metering features [54]. The manufacturing process is shown in Fig. 5. Firstly, photo etching creates unique platelet designs including channels, ridge, wall, side, end margin, and block end. This process employs corrosive oxidation of selected areas of metal and does not alter the internal structure of the metal or metal properties such as hardness, grain structure and ductility. The fluid flow passages of PCHE are mostly made of near-semicircular channels, with etch depth varying from 0.1 mm to 2.5 mm, and channel width varying from 0.2 mm to 5 mm. The passage shape may be corrugated or straight, depending on many factors, such as the working fluid to be used, the heat load, and the pressure drop requirements. The flexibility of the etching process can use any angle increments (1° or less) over a wide range, unlike fins, which are usually manufactured at set angles [56].

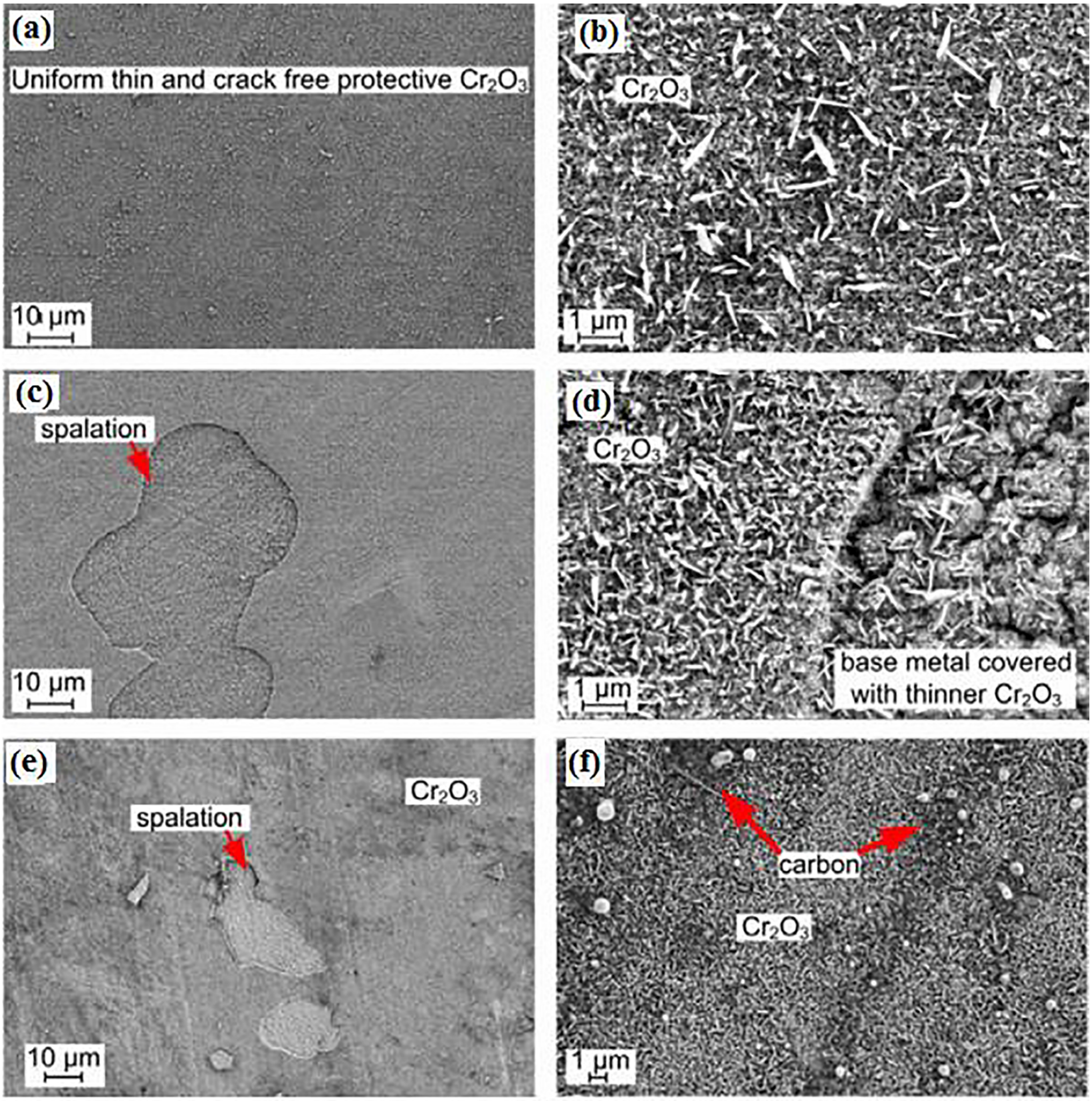

Fig. 4. Surface oxide morphology of Alloy 625 samples exposed to supercritical CO_2 for (a–b) 500 h, (c–d) 1000 h and (e–f) 3000 h [48].

Secondly, platelets are accurately stacked in a clean-room environment by maintaining heat and pressure in a controlled atmosphere to remove surface impurities and to promote grain growth across the interface between components. Then, diffusion bonding is applied to form a monolithic part where the bonding of flow plates, taking place in a high-temperature, high-pressure environment with no melting or deformation of channels, ensures flow integrity and complete bonding of all plates throughout the stack. This process uses no interlayer, flux, or braze alloy, and the interfacial area between two metal flow plates becomes welded together as atoms intertwine with one another, allowing for the incredibly precise construction of the internal flow passages within the block. As a result, this creates an extremely high-integrity solid block of the parent metal that contains the internally bound flow channels running throughout the core of the block [57,58]. Table 2 lists the diffusion-bonding process parameters. Among these parameters, three bonding variables, the bonding temperature, the bonding pressure and the holding time, primarily govern the success or failure of diffusion bonding. The bonding temperature is typically 0.6–0.7 of the absolute melting point of the material being bonded. The bonding pressure must be sufficiently low with respect to the yield strength of the material so that no large-scale deformation of the parts to be joined occurs. Holding times can vary from a few minutes to several hours [59,60]. The final process is assembly with the inlet/outlet flow distribution headers, which are welded on to the diffusion-bonded blocks. In this process, much attention should be given to large thermal gradients and possible residual stresses from the welding process, which can result in separation in adjacent areas between the header and the diffusion-bonded weld joint. To reduce/avoid any potential thermal gradients and localized thermal stresses during welding, brazing may be employed to join external flanges and headers to the diffusion-bonded assembly.

4. Thermohydraulic performance

So far, there are four main types of PCHE flow passage that have been developed: straight channel, zigzag (or wavy) channel, channel

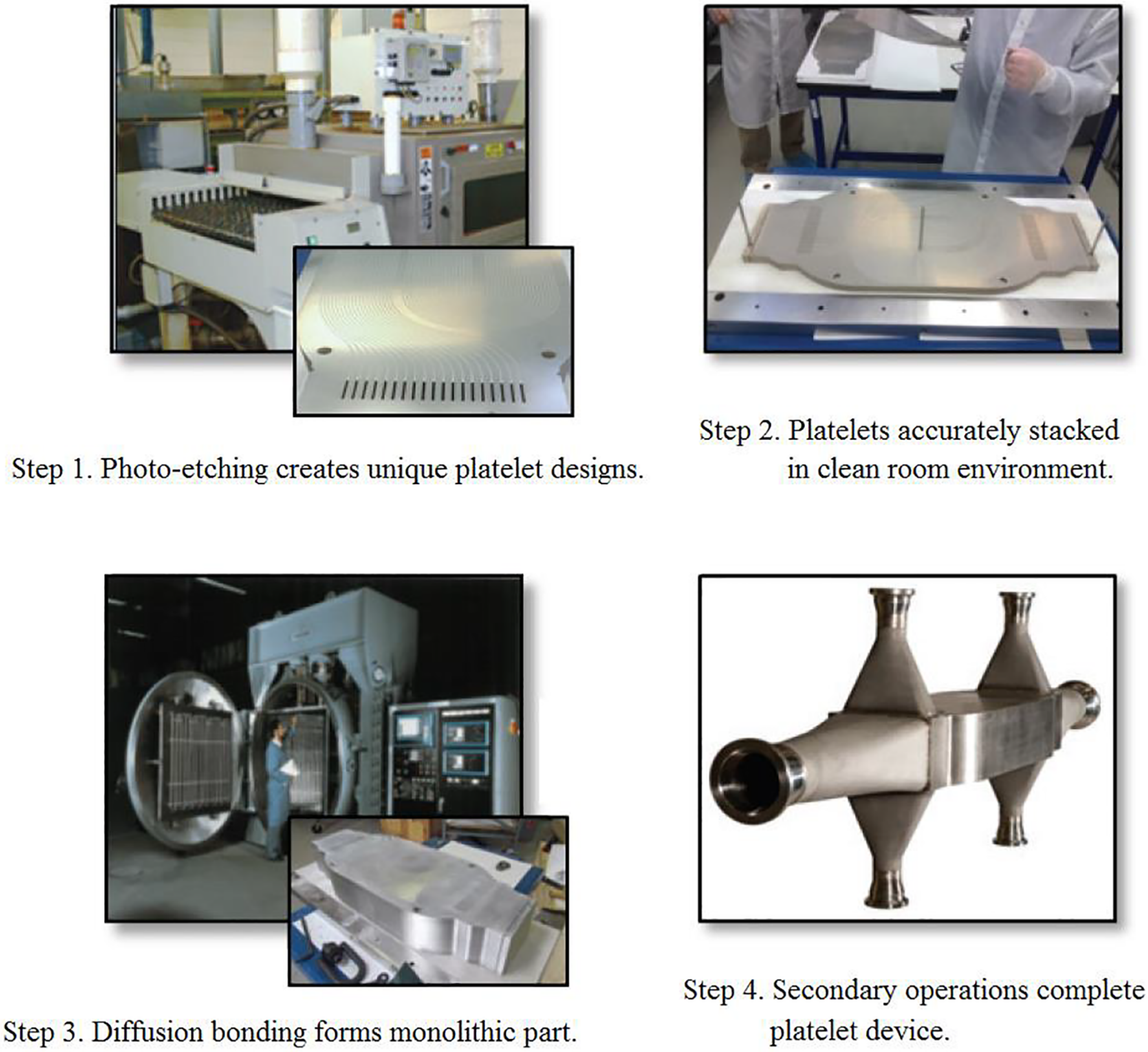

Fig. 5. PCHE manufacturing process [55].

Table 2
Diffusion-bonding process parameters [59].

Variables	Explanation
Material	Determining the required temperature and time for a diffusion joint to form.
Time	Determining the required time for diffusion welding.
Temperature	Diffusion welding occurring in the same range as recrystallization, about 0.6–0.7 melting temperature on an absolute temperature scale.
Pressure	A certain amount of pressure needed to produce intimate contact between opposing asperities.
Surface preparation	A thin layer of electroplated or vacuum-deposited material to protect the surface.
Filler material	Producing a completely uniform joint, indistinguishable from the base metal.

with S-shaped fins, and channel with airfoil fins, as shown in Fig. 6. In this section, we will focus on the thermohydraulic performance of these four types of PCHE.

4.1. Straight-channel PCHE

A summary of studies on the thermohydraulic performance of straight-channel PCHEs is shown in Table 3 in chronological order.

Mylavarapu et al. [61,62,63] designed and built a high-temperature helium test facility at Ohio State University in 2008, with the primary purpose of investigating the heat transfer and pressure drop characteristics of PCHE. The test facility was designed to facilitate operation at temperatures and pressures up to 900 °C and 3 MPa, respectively. A straight-channel PCHE, having ten hot and ten cold plates with twelve channels in each plate, was fabricated using Alloy 617 plates as shown in Fig. 7. A simplified steady state laminar PCHE computational model was developed, consisting of ten hot-side and ten cold-side plates, each 1.6 mm thick, with one straight channel per plate. Numerical investigations were conducted for various hydrodynamic entrance region parameters, such as incremental pressure drop number, apparent Fanning friction factor and hydrodynamic entrance length in a semi-circular duct. Results showed a much earlier Reynolds number of about 1700, marking the onset of transition from laminar to the transition flow regime and the non-dimensional hydrodynamic entrance length

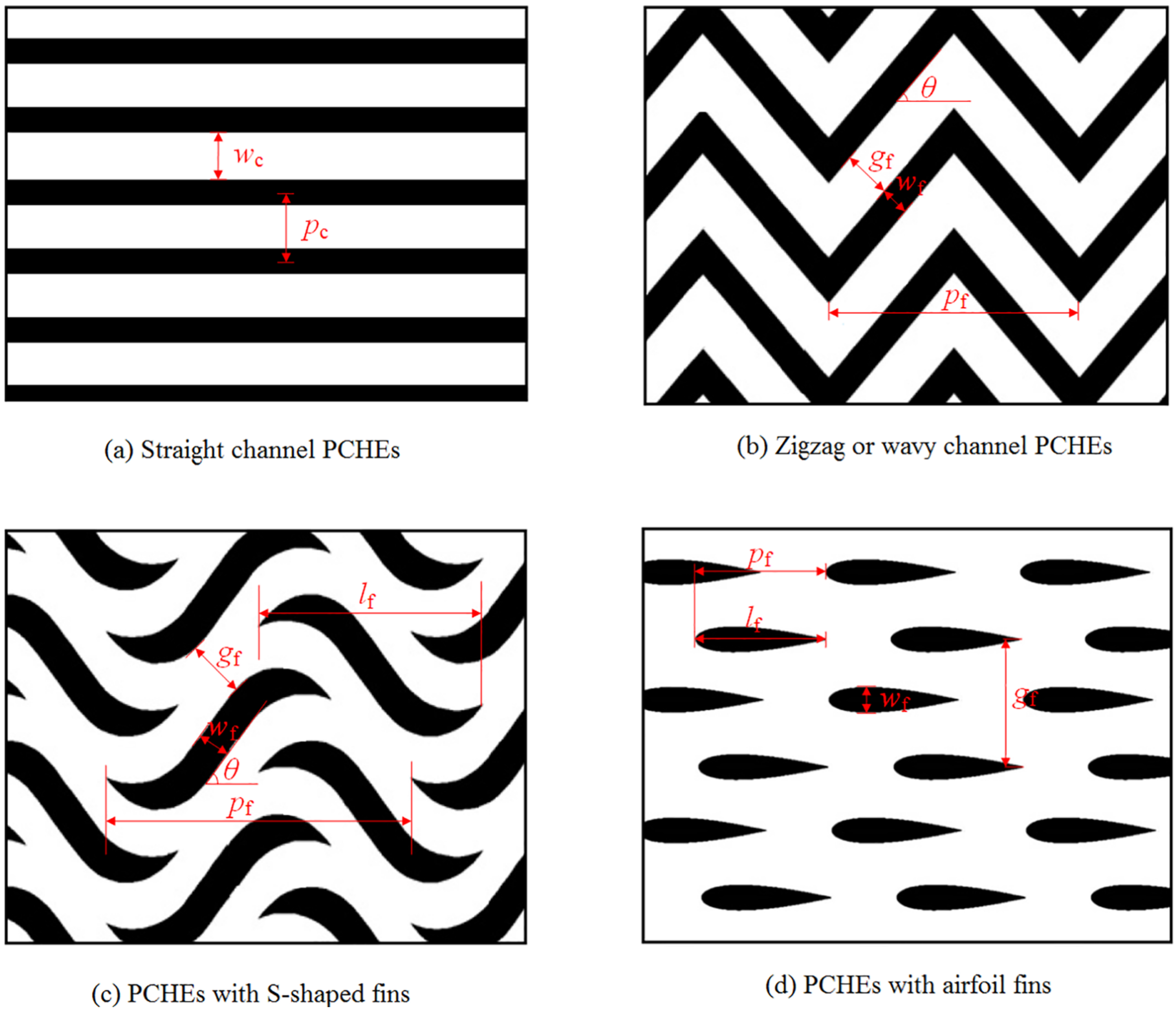

Fig. 6. Four main types of PCHEs (a) with straight channels, (b) with zigzag (or wavy) channels, (c) with S-shaped fins, and (d) with airfoil fins [20,60].

0.07–0.08 for laminar flow through a semi-circular duct. For hydrodynamically and thermally fully developed laminar flow through a semi-circular duct with an axially constant wall heat flux boundary condition, they recommended the correlations in the literature [68] with $fRe = 15.767$ and $Nu_{H1} = 4.089$. For transition and turbulent flow through straight semi-circular channels, the correlations given by Gnielinski [69] and Abraham et al. [70] were suggested for estimating the Nusselt number and the Fanning friction factor. The Gnielinski correlation [69] was developed for circular pipes for $2300 \le Re \le 5 \times 10^6$ and $0.5 \le Pr \le 2000$.

$$Nu_{H1} = \frac{(f/2)(Re - 1000)Pr}{1 + 12.7(Pr^{2/3} - 1)\sqrt{f/2}} \tag{1}$$

$$f = \frac{1}{4}\left(\frac{1}{1.82\log Re - 1.64}\right)^2 \tag{2}$$

where Nu and Re are calculated based on the channel hydraulic diameter. For $2300 \le Re \le 3100$, Abraham et al. [70] recommended the following correlation instead of the Gnielinski correlation:

$$Nu_{H1} = 3.5239\left(\frac{Re}{1000}\right)^4 - 45.148\left(\frac{Re}{1000}\right)^3 + 212.13\left(\frac{Re}{1000}\right)^2 - 427.45\left(\frac{Re}{1000}\right) + 316.08 \tag{3}$$

Chen et al. [65] developed two heat transfer correlations for their tested PCHE based on the steady-state experimental data using a direct method and an indirect method. The heat transfer correlation with a power function of the Reynolds number for a total of 182 data points on both the hot and cold sides, was proposed as

$$Nu = \begin{cases} (0.01352 \pm 0.0094)Re^{(0.80058 \pm 0.0921)} & \text{for } 1200 \leqslant Re \leqslant 1850 \\ (3.6361 \times 10^{-4} \pm 7.855 \times 10^{-5})Re^{(1.2804 \pm 0.0273)} & \text{for } 1850 < Re \leqslant 2900 \end{cases} \tag{4}$$

The heat transfer correlation from a nonlinear regression approach for a total of 76 data points on both the hot and cold sides, were obtained as

$$Nu = \begin{cases} (0.047516 \pm 0.015662)Re^{(0.633151 \pm 0.044606)} \quad \text{for } 1200 \leqslant Re \leqslant 1850 \\ (3.680123 \times 10^{-4} \pm 1.184389 \times 10^{-4})Re^{(1.282182 \pm 0.042068)} \\ \quad \text{for } 1850 < Re \leqslant 2900 \end{cases} \tag{5}$$

As shown in Fig. 8, comparison of the overall heat transfer coefficients (U) obtained from these developed correlations with experimental data shows good agreement. It should be pointed out that the conclusions above about equations 1–5 are from their operating temperature and pressure respectively larger than 85 °C and 1 MPa, which are far away from the helium critical point (-267.96 °C and 0.2276 MPa). When the operating condition near the critical or pseudo critical points, the above equations may not be applicable and should be modified by the effect of variable physical properties.

Researchers from Korea, China and India also studied the

Table 3
Representative thermohydraulic performance studies of straight-channel PCHEs.

Reference	Test section description			Test conditions		Measured characteristics
	Typical description	Hot-side configuration	Cold-side configuration	Hot side	Cold side	
Mylavarapu et al. [62]	Alloy 617 Counter-current flow	l_c: 0.305 m p_c: 2.5 mm w_c: 2 mm d_c: 1 mm n: 120 D_h: 1.22 mm A: 0.188 m^2	l_c: 0.272 m p_c: 2.5 mm w_c: 2 mm d_c: 1 mm n: 120 D_h: 1.22 mm A: 0.168 m^2	Helium $\dot{m}$: 15, 40, 80 kg/h T_{in}: 900 °C P_{out}: 3 MPa	Helium $\dot{m}$: 15, 40, 80 kg/h T_{in}: 540 °C P_{out}: 3 MPa	Numerical simulation Pressure drop Overall heat-transfer coefficient
Mylavarapu et al. [63]	Alloy 617 Counter-current flow	l_c: 0.305 m p_c: 2.5 mm w_c: 2 mm d_c: 1 mm n: 120 D_h: 1.22 mm A: 0.188 m^2	l_c: 0.272 m p_c: 2.5 mm w_c: 2 mm d_c: 1 mm n: 120 D_h: 1.22 mm A: 0.168 m^2	Helium $\dot{m}$: 10–49 kg/h T_{in}: 208–790 °C P_{in}: 1–2.7 MPa	Helium $\dot{m}$: 10–49 kg/h T_{in}: 85–390 °C P_{in}: 1–2.7 MPa	Both experiment and simulation Pressure factor Nusselt number
Figley et al. [64]	Alloy 617 Counter-current flow	l_c: 0.247 m w_c: 2 mm d_c: 1 mm n: 10 D_h: 1.22 mm A: 0.0127 m^2	l_c: 0.247 m w_c: 2 mm d_c: 1 mm n: 10 D_h: 1.22 mm A: 0.0127 m^2	Helium $\dot{m}$: 10–80 kg/h T_{in}: 1173 K P_{out}: 3 MPa	Helium $\dot{m}$: 10–80 kg/h T_{in}: 813 K P_{out}: 3 MPa	Numerical simulation Heat load Overall heat-transfer coefficient Thermal effectiveness
Seo et al. [10]	SUS304L Dimensions of 141 × 40 × 16 mm^3 Counter-current and parallel flow	p_c: 1.4 mm w_c: 0.8 mm d_c: 0.6 mm n: 66/110 D_h: 0.6685 mm A: 26,037 mm^2	p_c: 1.4 mm w_c: 0.8 mm d_c: 0.6 mm n: 88/132 D_h: 0.6685 mm A: 34,716 mm^2	Water Re: 100–850 T_{in}: 40–50 °C	Water Re: 100–550 T_{in}: 20 °C	Experiment data Pressure drop Pressure factor Heat-transfer rate Overall heat-transfer coefficient
Chen et al. [65]	Alloy 617 Dimensions of 305 × 102 × 73 mm^3 Counter-current flow	l_c: 0.305 m p_c: 2.54 mm w_c: 2 mm d_c: 1 mm n: 120 D_h: 1.22 mm A: 0.188 m^2	l_c: 0.272 m p_c: 2.54 mm w_c: 2 mm d_c: 1 mm n: 120 D_h: 1.22 mm A: 0.168 m^2	Helium $\dot{m}$: 22–39 kg/h T_{in}: 199–450 °C P_{in}: 1–2.7 MPa	Helium $\dot{m}$: 22–39 kg/h P_{in}: 1–2.7 MPa	Both experiment and simulation Local temperature Pressure factor Nusselt number
Aneesh et al. [66]	Alloy 617 Counter-current flow	l_c: 247.2 mm p_c: 3.6 mm w_c: 2 mm d_c: 1 mm D_h: 1.22 mm	l_c: 247.2 mm p_c: 3.6 mm w_c: 2 mm d_c: 1 mm D_h: 1.22 mm	Helium $\dot{m}$: 15–55 kg/h T_{in}: 973–1173 °C P_{in}: 1–9 MPa	Helium $\dot{m}$: 15–55 kg/h T_{in}: 613–1013 °C P_{in}: 1–9 MPa	Both experiment and simulation Local temperature and velocity profiles Thermal–hydraulic performance
Chu et al. [4]	SUS304L Counter-current flow	l_c: 150 mm p_c: 4 mm w_c: 2.8 mm d_c: 1.4 mm	l_c: 150 mm p_c: 4 mm w_c: 2.8 mm d_c: 1.4 mm	CO_2 $\dot{m}$: 150–650 kg/h T_{in}: 310–375 K P_{in}: 8–11 MPa	Water	Experiment data Pressure drop Pressure factor Heat-transfer rate Nusselt number
Kim et al. [67]	SUS304L Cross, parallel, and counter-current flow	l_c: 0.05–1.2 m p_c: 3 mm d_c: 0.5–2.5 mm	l_c: 0.05–1.2 m p_c: 3 mm d_c: 0.5–2.5 mm	LNG flue gas T_{in}: 500 °C	CO_2 T_{in}: 450 °C	Numerical simulation Heat-transfer capacity Heat-transfer effectiveness

thermohydraulic performance of straight-channel PCHE, both experimentally and numerically. For experimental studies, Seo et al. [10] built an experimental rig, fabricated a straight-channel PCHE and carried out the thermohydraulic performance analyses for Reynolds numbers in the range of 100–850. Results showed that average heat transfer rate and overall heat transfer coefficient of the counter-current configuration were 6.8% and 10–15% higher, respectively, than those of the parallel flow. Increasing Reynolds number was shown to lead to improved heat transfer performance, but also to a larger pressure drop, while increasing inlet temperature did not affect the heat transfer performance but did slightly decrease the pressure drop. Empirical heat transfer correlations of the hot and cold sides using the modified Wilson plot method were proposed as

$$Nu = 0.7203Re^{0.1775}Pr^{1/3}(\mu/\mu_w)^{0.14} \text{ for } 100 < Re < 850 \tag{6}$$

and the Fanning friction factor correlation, represented by the function of the Reynolds number was developed as follows:

$$f = 1.3383Re^{-0.5003} \text{ for } 100 < Re < 850 \tag{7}$$

The heat transfer correlations can be predicted from the experimental data within ± 7% error, while the friction factor correlation can be predicted within ± 8% error. Chu et al. [4] conducted a supercritical CO_2 experimental system and manufactured a straight-channel PCHE. They tested the effects of thermal properties, operating pressure and the pseudocritical point of CO_2 on the thermohydraulic performance of their PCHE and concluded that supercritical CO_2 had better heat transfer capability than water fluid, with the higher-pressure conditions leading to improved overall heat transfer performance, but operation at the transcritical state significantly reduced the thermohydraulic performance. The Nusselt number and Darcy friction factor correlations were fitted by experimental data in order to simplify the design process as follows.

For water turbulent flow:

$$Nu = 0.122Re^{0.56}Pr^{0.14} \tag{8}$$

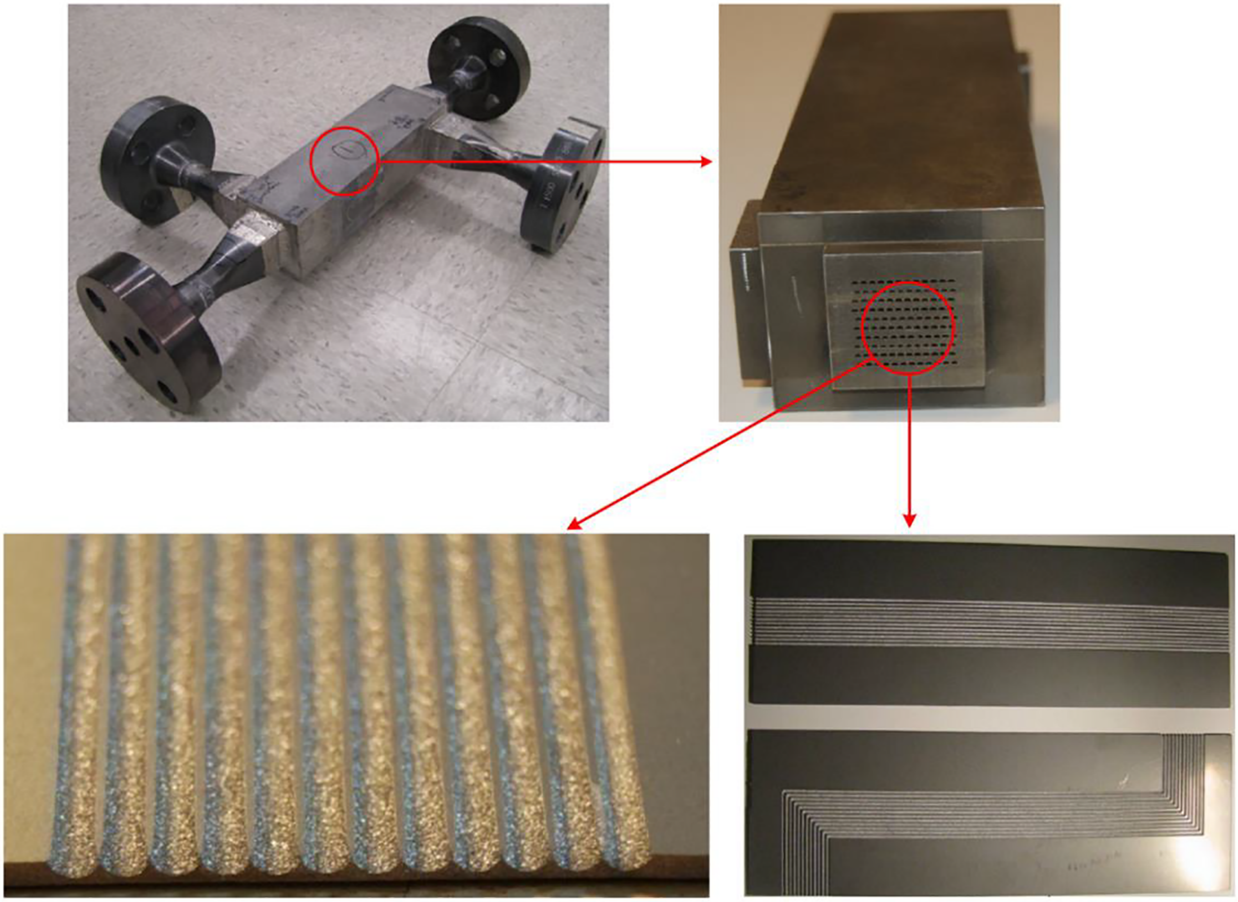

Fig. 7. A straight-channel PCHE tested at Ohio State University [61].

$$f = (1.12\ln(Re) + 0.85)^{-2} \tag{9}$$

For CO_2 in both the supercritical and transcritical states:

$$Nu = Nu_{fc} f(B) \tag{10}$$

$$f(B) = \begin{cases} 0.58 - 53\left(\frac{Gr}{Re^{2.7}}\right)^{0.36} \text{ for } T_w \approx T_{pc},\ \ 3\times 10^4 < Re < 6\times 10^4 \\ 0.36 - 22\left(\frac{Gr}{Re^{2.7}}\right)^{0.42} \text{ for } T_w > T_{pc},\ \ 3\times 10^4 < Re < 7\times 10^4 \end{cases} \tag{11}$$

$$Nu_{fc} = 0.0183 Re^{0.82} Pr^{0.5} \left(\frac{\rho}{\rho_w}\right)^{-0.3} \tag{12}$$

$$Gr = \frac{(\rho - \bar{\rho_w})\rho g D^3}{\mu^2} \tag{13}$$

$$\bar{\rho_w} = \frac{\rho(T - T_{pc}) + \rho_w(T_{pc} - T_w)}{T - T_w} \tag{14}$$

For numerical simulation, Aneesh et al. [66] carried out three-

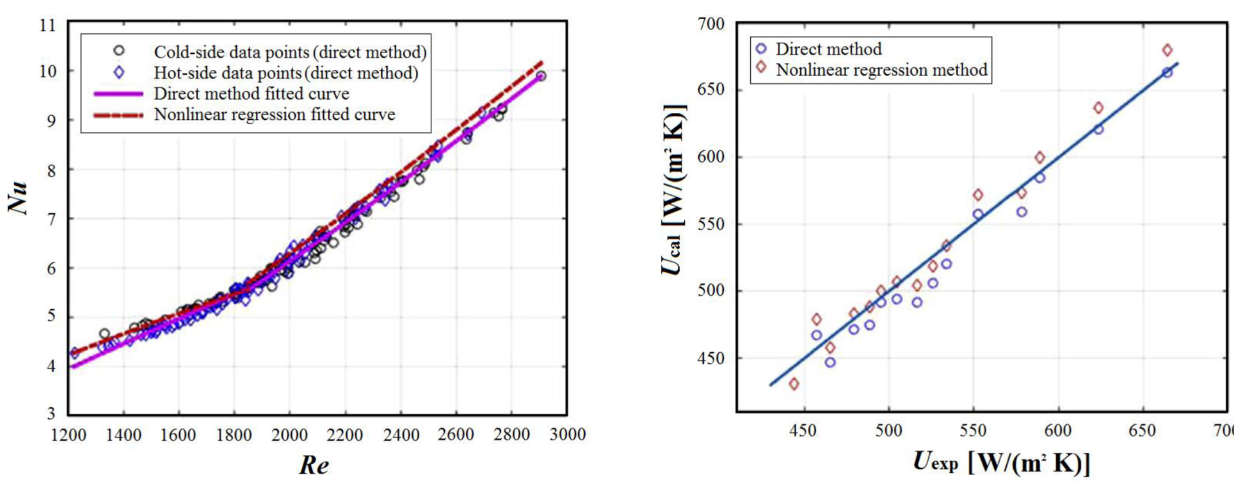

(a) (b)

Fig. 8. Comparison of the overall heat transfer coefficients obtained from fitted correlations and experiments for a straight-channel PCHE [65].

dimensional (3D) steady-state conjugate heat transfer simulations to examine the effect of variation of thermophysical properties and operating conditions on thermohydraulic performance, using helium as the working fluid and Alloy 617 as the solid substrate. Results showed the almost same performance for the aligned and staggered arrangements of the hot and cold channels in the PCHE and a better performance for single than double banking. Kim et al. [67] proposed a mathematical expression for the conduction and convection thermal resistances of cross, parallel, and counterflow PCHEs with straight channels, based on an extensive numerical study. In their model, the conduction heat transfer between the hot and cold channels in the PCHE was characterized by the conduction shape factor and the convection heat transfer performance in the semicircular channels was also expressed as a function of Graetz number ($Gz_D^{-1} = \frac{x}{DRePr}$). Fig. 9a and 9b show the effect of channel size and channel length, respectively, on the heat transfer effectiveness of the PCHE for three flow types. Among the three flow types, the counterflow type shows the best thermal performance, followed by the crossflow type, while the parallel flow type shows the worst performance.

4.2. Zigzag (or wavy)-channel PCHE

A summary of studies on the thermohydraulic performance of zigzag (or wavy) channel PCHEs is shown in Table 4 in chronological order.

In 2004, an experimental facility was built at the Tokyo Institute of Technology to investigate the thermohydraulic parameters of supercritical CO_2 for PCHE with zigzag channels. Nikitin et al. [71–73] investigated both experimentally and numerically the heat transfer and pressure drop characteristics of the zigzag-channel PCHE. The tested overall heat transfer coefficient varied from 300 to 650 W/(m^2 K), while the compactness of the heat exchanger core was about 1050 m^{-1} and the maximum power density approached 4.4 MW/m^3. Based on the experimental and numerical results, empirical correlations for heat transfer coefficient and pressure drop factor were proposed using a power function as illustrated below:

$$h_{hot} = 2.52Re^{0.681} \text{ for } 2800 < Re < 5800 \quad (15)$$

$$h_{cold} = 5.49Re^{0.625} \text{ for } 6200 < Re < 12100 \quad (16)$$

$$f_{hot} = (-1.402 \times 10^{-6} \pm 0.087 \times 10^{-6})Re^{+(0.04495 \pm 0.00038)} \text{ for } 2800 < Re < 5800 \quad (17)$$

$$f_{cold} = (-1.545 \times 10^{-6} \pm 0.099 \times 10^{-6})Re^{+(0.09318 \pm 0.0009)} \text{ for } 6200 < Re < 12100 \quad (18)$$

The calculation of *Re* is based on the channel hydraulic diameter. It can be noted that all four correlations are independent of *Pr*. However, the heat transfer coefficient should be associated with *Pr*, as a result of the change in the ratio of momentum diffusivity to thermal diffusivity, and so the above four correlations are not universal and their application is limited to the same geometry parameters and operating conditions as those of Nikitin et al. [71–73]. Ngo et al. [60,74] also realised this problem and ascribed these independencies to the narrow range of $0.75 < Pr < 1.04$. To address this, a zigzag PCHE was investigated by varying *Pr* widely, from 0.75 to 2.2. The results confirmed Nusselt number dependence on *Pr*. However, the Fanning friction factor was found to be independent of *Pr*.

$$Nu = (0.1696 \pm 0.0144)Re^{0.629 \pm 0.009}Pr^{0.317 \pm 0.014} \text{ for } 3.5 \times 10^3 < Re < 2.2 \times 10^4, \ 0.75 < Pr < 2.2 \quad (19)$$

$$f = (0.1924 \pm 0.0299)Re^{-0.091 \pm 0.016} \text{ for } 3.5 \times 10^3 < Re < 2.2 \times 10^4 \quad (20)$$

As shown in Fig. 10a and 10b, these empirical correlations can predict the overall heat transfer coefficient and pressure drop very well, with a standard deviation of ± 3% and ± 13.5%, respectively. Following on from the work at Tokyo Institute of Technology, Lee and Kim [79–82] from Inha University focused on the effects of the geometric parameters of zigzag flow channels on the performance of a PCHE based on 3D Reynolds-averaged Navier–Stokes analysis with the shear stress transport (SST) turbulence model. The studied geometric parameters included the channel angle, the ellipse aspect ratio of the channel, the ratios of the pitch and depth of the ribs to the hydraulic diameter of the channel, and four different shapes of channel cross section (semicircular, rectangular, trapezoidal, and circular) and configuration. The results demonstrated that the rectangular channel showed the best thermal performance coupled with the worst hydraulic performance, while the circular channel showed the worst thermal performance.

In 2008, a helium test loop was constructed at Korea Advanced Institute of Science and Technology to investigate the thermohydraulic performance of PCHE for application to helium high temperature gas-cooled reactors. Kim and No [76–78] measured the pressure drop and temperature difference at the inlet and outlet of the hot and cold sides of a PCHE and proposed the following Nusselt number and Fanning factor correlations:

$$Nu = 3.255 + 0.00729(Re - 350) \text{ for } 350 < Re < 800, \ Pr = 0.66 \quad (21)$$

$$fRe = 16.51 + 0.01627Re \text{ for } 350 < Re < 1200 \quad (22)$$

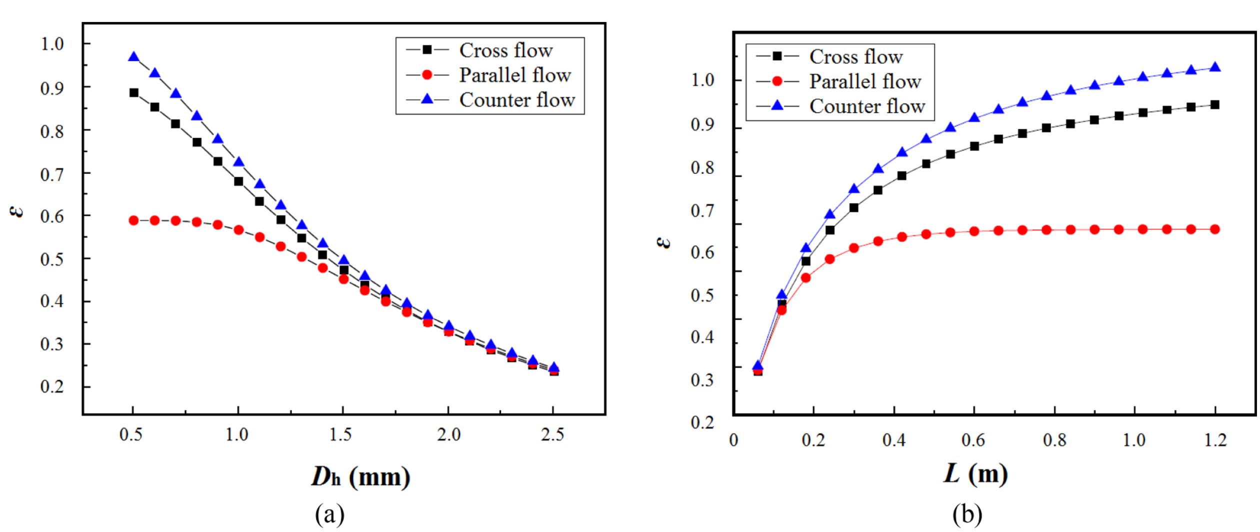

Fig. 9. Effect of channel sizes (a) and channel length (b) on heat transfer effectiveness [67].

Table 4
Representative thermohydraulic performance studies of zigzag (or wavy)-channel PCHEs.

Reference	Test section description			Test conditions		Measured characteristics
	Typical description	Hot-side configuration	Cold-side configuration	Hot side	Cold side	
Nikitin et al. [71–73]	Core dimensions of 71 × 76 × 896 mm^3 A dry mass of 40 kg Counter-current flow	θ: 32.5° p_f: 9 mm g_f: 1.9 mm w_f: 0.6 mm l: 1000 mm n: 144 D_h: 1.9 mm A: 0.697 m^2	θ: 40° p_f: 7.24 mm g_f: 1.8 mm w_f: 0.7 mm l: 1100 mm n: 66 D_h: 1.8 mm A: 0.356 m^2	CO_2 $\dot{m}$: 40–80 kg/h T: 280–300 °C P: 2.2–3.2 MPa	CO_2 $\dot{m}$: 40–80 kg/h T: 90–108 °C P: 6.5–10.5 MPa	Both experiment and simulation Heat transfer coefficient and effectiveness Pressure factor Overall heat transfer coefficient
Ngo et al. [74]	316L stainless steel Dimensions of 745.2 × 76 × 29 mm^3 Counter-current flow	θ: 52° p_f: 7.565–3.426 mm g_f: 1.31 mm w_f: 0.8 mm d_c: 0.94 mm n: 96 D_h: 1.09 mm A: 0.4653 m^2	θ: 52° p_f: 7.565–3.426 mm g_f: 1.31 mm w_f: 0.8 mm d_c: 0.94 mm n: 44 D_h: 1.09 mm A: 0.2353 m^2	CO_2 $\dot{m}$: 30–85 kg/h T_{in}: 280 °C P_{in}: 6.5–10.5 MPa	CO_2 $\dot{m}$: 30–85 kg/h T_{in}: 108 °C P_{in}: 2.2–3.5 MPa	Experiment data Pressure factor Nusselt number
Ngo et al. [60]	316L stainless steel Dimensions of 745.2 × 76 × 29 mm^3 Counter-current flow	θ: 52° p_f: 7.565–3.426 mm g_f: 1.31 mm w_f: 0.8 mm d_c: 0.94 mm n: 96 D_h: 1.09 mm A: 0.4653 m^2	θ: 52° p_f: 7.565–3.426 mm g_f: 1.31 mm w_f: 0.8 mm d_c: 0.94 mm n: 44 D_h: 1.09 mm A: 0.2353 m^2	CO_2 $\dot{m}$: 40–150 kg/h T_{in}: 120 °C P_{in}: 6 MPa	CO_2 $\dot{m}$: 40–150 kg/h T_{in}: 35–55 °C P_{in}: 7.7–12 MPa	Experiment data Pressure factor Nusselt number
Kim et al. [75]	Dimensions of 846 × 7.74 × 4.89 mm^3 Counter-current flow	θ: 32.5° p_f: 9 mm g_f: 1.9 mm w_f: 0.6 mm n: 2	θ: 40° p_f: 7.24 mm g_f: 1.8 mm w_f: 0.7 mm n: 1	CO_2 $\dot{m}$: 0.0001445 kg/s T_{in}: 279.9 °C P_{out}: 2.52 MPa	CO_2 $\dot{m}$: 0.0003152 kg/s T_{in}: 107.9 °C P_{out}: 8.28 MPa	Numerical simulation Flow-velocity profile Pressure drop Heat transfer rate
Kim et al. [76]	Alloy 800H Dimensions of 896 × 150 × 144 mm^3 Dry mass 146 kg Counter-current flow	θ: 15° p_f: 24.6 mm l_c: 765 mm n: 1280 d: 1.51 mm D_h: 0.922 mm A: 3.8 m^2	θ: 15° p_f: 24.6 mm l_c: 765 mm n: 1280 d: 1.51 mm D_h: 0.922 mm A: 3.8 m^2	Helium $\dot{m}$: 40–100 kg/h T_{in}: 25–550 °C P_{in}: 1.5–1.9 MPa	Helium $\dot{m}$: 40–100 kg/h T_{in}: 25–100 °C P_{in}: 1.5–1.9 MPa	Both experiment and simulation Temperature profile along flow direction Heat flux along flow direction Pressure factor Nusselt number
Kim and No [77]	Alloy 800H Dimensions of 896 × 150 × 144 mm^3 Dry mass 146 kg Counter-current flow	θ: 15° p_f: 24.6 mm l_c: 765 mm n: 1280 d: 1.51 mm D_h: 0.922 mm A: 3.8 m^2	θ: 15° p_f: 24.6 mm l_c: 765 mm n: 1280 d: 1.51 mm D_h: 0.922 mm A: 3.8 m^2	Helium $\dot{m}$: 65–120 kg/h T_{in}: 80–240 °C P_{in}: 1.75–1.78 MPa	Water $\dot{m}$: 8–45 kg/h T_{in}: 10–26 °C P_{in}: 0.1–0.51 MPa	Both experiment and simulation Pressure factor Nusselt number
Kim and No [78]	Alloy 800H Dimensions of 896 × 150 × 144 mm^3 Dry mass 146 kg Counter-current flow	θ: 5–45° p_f: 12.3–24.6 mm l_c: 765 mm n: 1280 D_h: 0.922–1.222 mm	θ: 5–45° p_f: 12.3–24.6 mm l_c: 765 mm n: 1280 D_h: 0.922–1.222 mm	Helium $\dot{m}$: 40–100 kg/h T_{in}: 25–550 °C P_{in}: 1.5–1.9 MPa	Helium $\dot{m}$: 40–100 kg/h T_{in}: 25–100 °C P_{in}: 1.5–1.9 MPa	Numerical simulation Pressure factor Nusselt number
Lee and Kim [79–82]	Counter-current flow	θ: 32.5° p_f: 9 mm g_f: 1.9 mm w_f: 0.6 mmv D_h: 1.9 mm	θ: 0–45° p_f: 7.24 mm g_f: 0.9–2.88 mm w_f: 0.7 mm D_h: 1.8 mm	CO_2 Re: 71500 T_{in}: 138.2 °C P_{in}: 2.528 MPa	CO_2 Re: 152000 T_{in}: 123 °C P_{in}: 8.312 MPa	Numerical simulation Flow-velocity profile Pressure factor Heat transfer effectiveness
Lee and Kim [83,84]	Counter-current flow Four shapes of channel cross sections and three configurations	θ: 32.5° p_f: 9 mm g_f: 1.9 mm w_f: 0.6 mm	θ: 40° p_f: 7.24 mm g_f: 1.8 mm w_f: 0.7 mm	CO_2 Re: 71500 T_{in}: 138.2 °C P_{in}: 2.528 MPa	CO_2 Re: 65000–270000 T_{in}: 123 °C P_{in}: 8.312 MPa	Numerical simulation Flow-velocity profile Pressure factor Heat transfer effectiveness
Bartel et al. [85]	Counter-current flow	θ: 0–20° p_f: 24.6 mm w_f: 1.51 mm D_h: 0.922 mm	θ: 0–20° p_f: 24.6 mm w_f: 1.51 mm D_h: 0.922 mm	Helium $\dot{m}$: 450 kg/h T_{in}: 800 °C P_{in}: 7 MPa	Helium $\dot{m}$: 450 kg/h T_{in}: 520 °C P_{in}: 7.97 MPa	Design study Pressure drop Nusselt number
Ma et al. [86]	Counter-current flow	θ: 0–45° p_f: 24.6 mm d: 1.51 mm D_h: 0.922 mm	θ: 0–45° p_f: 24.6 mm d: 1.51 mm D_h: 0.922 mm	Helium $\dot{m}$: 0.072–0.324 kg/h T_{in}: 1173 K P_{out}: 0	Helium $\dot{m}$: 0.072–0.324 kg/h T_{in}: 813 K P_{out}: 0	Numerical simulation Local thermal–hydraulic performance Pressure factor Nusselt number Heat transfer effectiveness

(*continued on next page*)

Table 4 (*continued*)

Reference	Test section description			Test conditions		Measured characteristics
	Typical description	Hot-side configuration	Cold-side configuration	Hot side	Cold side	
Khan et al. [87]	Alloy 617 Counter-current flow	θ: 0–15° d: 1.51 mm D_h: 0.922 mm	θ: 0–15° d: 1.51 mm D_h: 0.922 mm	Helium Re: 350–2100 T_{in}: 1173 K P_{out}: 3 MPa	Helium Re: 350–2100 T_{in}: 813 K P_{out}: 3 MPa	Numerical simulation Local thermal–hydraulic performance Pressure factor Nusselt number
Chen et al. [88]	Alloy 617 Dimensions of 339.1 × 126 × 50.8 mm^3 Counter-current flow	θ: 15° p_f: 24.6 mm d: 2 mm g_f: 0.5 mm	θ: 15° p_f: 24.6 mm d: 2 mm g_f: 0.5 mm	Helium $\dot{m}$: 22–39 kg/h T_{in}: 199–802 °C P_{in}: 1.6–2.7 MPa	Helium $\dot{m}$: 22–39 kg/h P_{in}: 1.6–2.7 MPa	Experiment data Pressure factor Nusselt number
Kim et al. [89]	316L stainless steel Dimensions of 54 × 2.2 × 4.89 mm^3 Counter-current flow	θ: 32.5° p_f: 9 mm g_f: 1.9 mm D_h: 1.9 mm	θ: 40° p_f: 7.24 mm g_f: 1.8 mm D_h: 1.8 mm	CO_2 $\dot{m}$: 30–400 kg/h T_{in}: 280 °C P_{in}: 3.2 MPa	CO_2 $\dot{m}$: 30–400 kg/h T_{in}: 108 °C P_{in}: 10.5 MPa	Numerical simulation Pressure factor Nusselt number
Baik et al. [7]	316L stainless steel Counter-current flow	p_f: 30–60 mm d: 1.5–2.1 mm a: 0–6 mm	p_f: 30–60 mm d: 1.5–2.1 mm a: 0–6 mm	LNG flue gas T_{in}: 923.15 K P_{in}: 0.106 MPa	CO_2 T_{in}: 497.15 K P_{in}: 13.6 MPa	Numerical simulation Flow-velocity and temperature profiles Pressure drop Heat transfer rate
Lee et al. [90]	316L stainless steel Counter-current flow	θ: 32.5° p_f: 9 mm g_f: 1.9 mm n: 2	θ: 40° p_f: 7.24 mm g_f: 1.8 mm n: 1	CO_2 $\dot{m}$: (1.41–2.48) × 10^{-4} kg/s T_{in}: 553.05 K P_{in}: 2.54 MPa	CO_2 $\dot{m}$: (1.41–2.48) × 10^{-4} kg/s T_{in}: 381.05 K P_{in}: 8.31 MPa	Numerical simulation Flow-velocity profiles Pressure drop Pressure factor Heat transfer coefficient
Yoon et al. [91]	Alloy 617	θ: 5–45° p_f: 5–40 mm n: 1 d: 2 mm D_h: 1.222 mm	θ: 5–45° p_f: 5–40 mm n: 1 d: 2 mm D_h: 1.222 mm	Helium Re: 100–2000	Helium Re: 100–2000	Numerical simulation Pressure factor Nusselt number

Next, a laminar 3D numerical solution with periodic boundary conditions was performed, with expanded Reynolds number up to 2500. Based on results validated against experimental data, the Nusselt number and Fanning factor correlations were modified as

$$Nu = 4.089 + 0.00365RePr^{0.58} \text{ for } Re < 2500 \tag{23}$$

$$fRe = 15.78 + 0.004868Re^{0.8416} - (10.939 - 11.014\nu_s/\nu) \text{ for } Re < 2500 \tag{24}$$

where ν_s/ν_b is the surface to bulk mean ratio of the viscosity. Finally, they used the numerical code to develop models for Fanning factor and Nusselt number for various geometries, including angle (from 5° to 45°), pitch length (between 12.3 mm and 24.6 mm), and diameter (from 1.51 mm to 2 mm) and developed correlations for Nusselt number and Fanning friction factor using local information produced by the numerical results, in the following form:

$$Nu = 4.089 + aRe^b \tag{25}$$

$$fRe = 15.78 + c\mathrm{Re}^d \tag{26}$$

where the constants a, b, c and d relate to the PCHE geometry and include the effects of angles, pitch, and hydraulic diameter. The relationship of Nusselt number to Reynolds number, and Fanning factor multiplied by Reynolds number to Reynolds number for a pitch of 24.6 mm and different channel angles is shown in Fig. 11a and b, respectively.

Kim et al. [89] created a k-ε SST turbulence model with CO_2 real gas properties to develop Nusselt number and Fanning friction factor

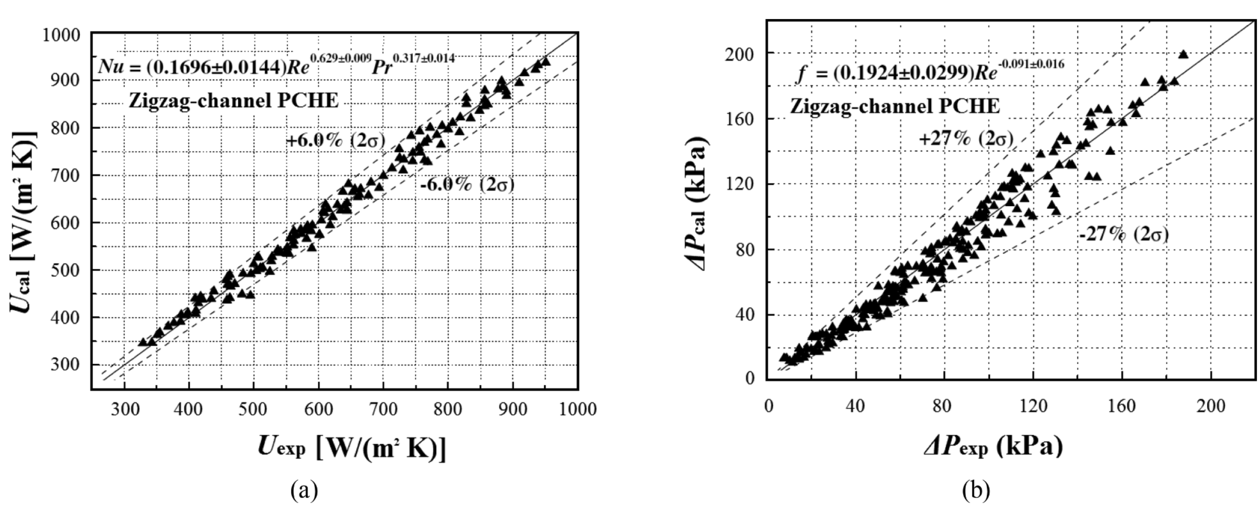

Fig. 10. Comparison of results obtained from proposed correlations and experiments for a zigzag-channel PCHE (a) overall heat transfer coefficient, and (b) pressure drop [60].

correlations covering an extended range of Reynolds numbers:

Correlations for $\theta = 32.5°$, $2000 < Re < 58000$, $0.7 < Pr < 1$, are:

$$Nu = (0.0292 \pm 0.0015)Re^{0.8138 \pm 0.005} \tag{27}$$

$$f = (0.2515 \pm 0.0097)Re^{-0.2031 \pm 0.0041} \tag{28}$$

and for $\theta = 40°$, $2000 < Re < 55000$, $0.7 < Pr < 1$,

$$Nu = (0.0188 \pm 0.0032)Re^{0.8742 \pm 0.0162} \tag{29}$$

$$f = (0.2881 \pm 0.0212)Re^{-0.1322 \pm 0.0079} \tag{30}$$

It should be noted that equations 27–30 are again independent of *Pr*, limiting their application to similar geometry parameters and operating conditions as those used by Kim et al. [89].

Researchers from USA, China and India have also carried out research in this field. For experimental studies, Chen et al. [88] fabricated a reduced-scale zigzag-channel PCHE using Alloy 617 plates for the heat exchanger core and experimentally investigated its pressure drop and heat transfer characteristics in the high-temperature helium test facility of Ohio State University. The maximum channel Reynolds number was approximately 3558, covering the laminar flow and laminar-to-turbulent flow transition regimes. Based on the experimental data, the heat transfer and pressure drop correlations were developed using the nonlinear regression method:

$$Nu = \begin{cases} (0.05516 \pm 0.00160)Re^{(0.69195 \pm 0.00559)} & \text{for } 1400 \leqslant Re \leqslant 2200 \\ (0.09221 \pm 0.01397)Re^{(0.62507 \pm 0.01949)} & \text{for } 2200 < Re \leqslant 3558 \end{cases} \tag{31}$$

$$f = \begin{cases} 17.639Re^{-(0.8861 \pm 0.0017)} & \text{for } 1400 \leqslant Re \leqslant 2200 \\ 0.019044 \pm 0.001692 & \text{for } 2200 < Re \leqslant 3558 \end{cases} \tag{32}$$

These two correlations only apply to the similar geometry parameters and operating conditions as those used for their development. Comparisons between the experimental data of the zigzag channels and the results obtained from the straight-channel PCHE by Figley et al. [64] indicated that the zigzag channels can lead to two to three times higher heat transfer coefficient in the laminar flow regime and one-and-a-half to three times higher in the transition flow regime compared to straight channels. For numerical studies, Ma et al. [86] and Khan et al. [87] conducted a 3D, laminar, incompressible and steady state model, respectively, to test the local heat transfer and pressure drop mechanism of zigzag-channel PCHE. They found that the local Nusselt number and friction factor at high temperature matched well with those at low temperature for Reynolds numbers larger than 900, and that the heat transfer and pressure drop both increased with an increase in the inclined angle within the range of 0–45°. Baik et al. [7] investigated the thermal performance of wavy-channel PCHE and the effects of the waviness factors, including the amplitude and the period, on the thermal performance. They concluded that wavy-channel PCHE can have significantly higher thermal performance than the straight-channel ones, mainly due to the increased area for heat transfer. To improve the performance of the zigzag-channel PCHE, Lee et al. [90] proposed a zigzag-type PCHE with inserted straight channels, as shown in Fig. 12, and conducted 3D numerical analysis with re-normalization group (RNG) k-ε model to examine its thermohydraulic performance. Through a comparison of the dimensionless factors, including Fanning friction factor, Colburn-j factor, and volume-goodness factor ($G_v = \frac{j}{f^{1/3}}$), the zigzag channel with the inserted straight channel showed an advanced thermohydraulic performance that was better than the regular zigzag or wavy channel. For example, for straight-channel lengths varying between 0.5 mm and 2 mm, the heat transfer characteristics of 1 mm straight channels were quite similar to those of the zigzag channel, but the Fanning friction factors were reduced by 60% for all of the mass flow rates, resulting in a volume-goodness factor that was improved by 26–28% compared to that of the original zigzag channel. Yoon et al. [91] conducted two laminar CFD models for investigation of the effects of geometric parameters such as relative length ratio, zigzag angle and radius of curvature of bend on thermohydraulic performance. A single channel isothermal model was used to investigate friction factors, while a two-channel model was used to study the Nusselt number in zigzag channels and the effect of temperature-dependent fluid properties on the pressure loss. The results showed that the friction factor of the zigzag channel was mainly influenced by the zigzag-channel geometry, while Nusselt number was dependent on the overall heat exchanger design, including the plenum sections. Based on the extensive CFD analysis database, Nusselt number and Fanning friction factor correlations were developed by implementing a least squares method:

for the region $200 \leq Re \leq 550$ and $5° \leq \theta \leq 15°$,

$$Nu = 5.05 + (0.02\theta + 0.003)RePr^{0.6} \tag{33}$$

while for the region $550 < Re \leq 2000$, $15° < \theta \leq 45°$,

$$Nu_{\mathrm{h}} = (0.71\theta + 0.289)(l_{\mathrm{R}}/D)^{-0.087}Re^{(-0.11(\theta-0.55)^2-0.004(l_{\mathrm{R}}/D)\theta+0.54)}Pr^{0.56} \tag{34}$$

$$Nu_{\mathrm{c}} = (0.18\theta + 0.457)(l_{\mathrm{R}}/D)^{-0.038}Re^{(-0.23(\theta-0.74)^2-0.004(l_{\mathrm{R}}/D)\theta+0.56)}Pr^{0.58} \tag{35}$$

These Nusselt number correlations are valid for $Pr \leq 1$ and $4.09 \leq l_{\mathrm{R}}/D_{\mathrm{h}} \leq 12.27$. For sharp-edged zigzag channels,

$$f_{\mathrm{app}} = \frac{15.78}{Re} + 0.0067268\exp(6.6705\theta)(l_{\mathrm{R}}/D)^{-2.3833\theta+0.26648} + 0.0435551\theta - 0.010814 \tag{36}$$

while for round-edged zigzag channels,

$$f_{\mathrm{app}} = \frac{15.78}{Re} + 0.029311\exp(1.9216\theta)(l_{\mathrm{R}}/D)^{-0.8261\theta+0.031254} + 0.047659\theta - 0.028674 \tag{37}$$

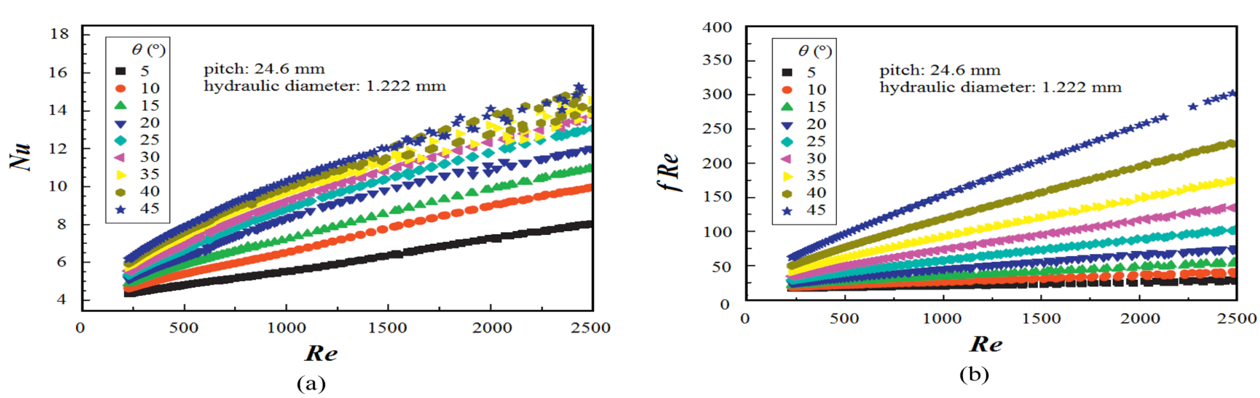

Fig. 11. Thermohydraulic performance of zigzag-channel PCHEs with different channel angles (a) Nusselt number vs. Reynolds number (b) Fanning factor multiplied by Reynolds number vs. Reynolds number [78].

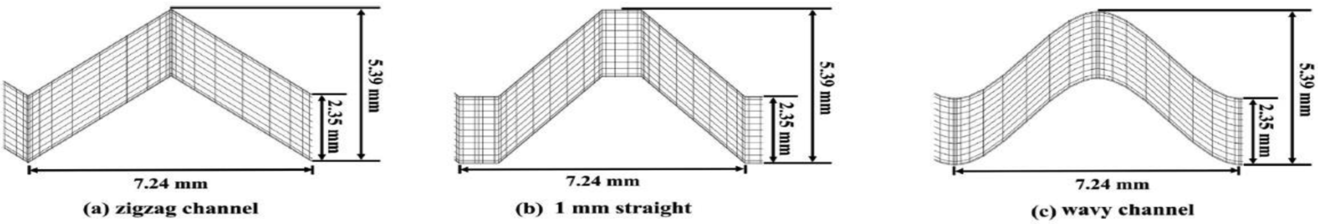

Fig. 12. Zigzag-channel PCHE (a) zigzag channel, (b) with inserted 1 mm straight channels and (c) wavy channel [90].

Table 5
Representative thermohydraulic performance studies of PCHEs with S-shaped fins.

Reference	Test section description			Test conditions		Measured characteristics
	Typical description	Hot-side configuration	Cold-side configuration	Hot side	Cold side	
Tsuzuki et al. [92,93]	Dimensions of 120 × 10 × 4.8 mm^3 Counter-current flow	θ: 0–57° p_f: 5.2–9.6 mm g_f: 2.7 mm w_f: 0.8 mm l_f: 2.6–4.8 mm d_c: 0.94 mm n: 24	θ: 0–57° p_f: 5.2–9.6 mm g_f: 2.7 mm w_f: 0.8 mm l_f: 2.6–4.8 mm d_c: 0.94 mm n: 11	CO_2 G: 42.1 kg/(m^2 s) T_{out}: 437.1–443.4 K	CO_2 G: 76.6 kg/(m^2 s) T_{out}: 489.9–496.3 K	Numerical simulation Flow-velocity profile Local heat transfer coefficient Heat transfer rate Pressure drop
Ngo et al. [94]	Copper Typical dimension of 136.17 × 18.56 × 7.26 mm^3 with variation among models Counter-current flow	θ: 52° p_f: 9.6 mm w_f: 0.4 mm g_f: 0.66–2.65 mm l_f: 4.8 mm d_c: 0.47–1.51 mm D_h: 0.55–1.92 mm	θ: 52° p_f: 28.8 mm w_f: 1.2 mm g_f: 6.17–10.22 mm l_f: 14.4 mm d_c: 2.5–5.0 mm D_h: 3.56–6.72 mm	CO_2 $\dot{m}$: 57.8 kg/h T_{in}: 118 °C T_{out}: 16 °C P: 11.5 MPa	Water $\dot{m}$: 48 kg/h T_{in}: 7 °C T_{out}: 90 °C P: 0.25 MPa	Numerical simulation Flow-velocity profile Local heat transfer coefficient Overall heat transfer coefficient
Nikitin et al. [74]	316L stainless steel Dimensions of 745.2 × 76 × 29 mm^3 Counter-current flow	θ: 52° p_f: 7.565–3.426 mm g_f: 1.31 mm w_f: 0.8 mm l_f: 1.713–3.783 mm d_c: 0.94 mm n: 96 D_h: 1.09 mm A: 0.5099 m^2	θ: 52° p_f: 7.565–3.426 mm g_f: 1.31 mm w_f: 0.8 mm l_f: 1.713–3.783 mm d_c: 0.94 mm n: 44 D_h: 1.09 mm A: 0.2559 m^2	CO_2 $\dot{m}$: 30–85 kg/h T_{in}: 280 °C P_{in}: 6.5–10.5 MPa	CO_2 $\dot{m}$: 30–85 kg/h T_{in}: 108 °C P_{in}: 2.2–3.5 MPa	Experiment data Pressure factor Nusselt number
Ngo et al. [60]	316L stainless steel Dimensions of 745.2 × 76 × 29 mm^3 Counter-current flow	θ: 52° p_f: 3.426–7.565 mm g_f: 1.31 mm w_f: 0.8 mm l_f: 1.713–3.783 mm d_c: 0.94 mm n: 96 D_h: 1.09 mm A: 0.5099 m^2	θ: 52° p_f: 7.565–3.426 mm g_f: 1.31 mm w_f: 0.8 mm l_f: 1.713–3.783 mm d_c: 0.94 mm n: 44 D_h: 1.09 mm A: 0.2559 m^2	CO_2 $\dot{m}$: 40–150 kg/h T_{in}: 120 °C P_{in}: 6 MPa	CO_2 $\dot{m}$: 40–150 kg/h T_{in}: 35–55 °C P_{in}: 7.7–12 MPa	Experiment data Pressure factor Nusselt number
Tsuzuki et al. [95]	Dimensions of 1,240 × 68 × 4.75 mm^3 Counter-current flow	θ: 52° p_f: 9.6 mm w_f: 0.4 mm g_f: 0.87 mm l_f: 4.8 mm d_c: 0.47 mm D_h: 0.61 mm	θ: 52° p_f: 28.8 mm w_f: 1.2 mm g_f: 6.17 mm l_f: 14.4 mm d_c: 2.5 mm D_h: 3.56 mm	CO_2 $\dot{m}$: (0.926–2.47) × 10^{-3} kg/s T_{in}: 120 °C P: 12 MPa	Water $\dot{m}$: (0.604–1.75) × 10^{-3} kg/s T_{in}: 5 °C P: 0.25 MPa	Numerical simulation Nusselt number Reynolds number Prandtl number
Tsuzuki et al. [96]	Dimensions of 120 × 10 × 4.8 mm^3 Counter-current flow	θ: 0–57° g_f: 2.7 mm w_f: 0.2–1 mm l_f: 2.4–9.6 mm d_c: 0.94 mm n: 2	θ: 0–57° g_f: 2.7 mm w_f: 0.2–1 mm l_f: 2.4–9.6 mm d_c: 0.94 mm n: 1	CO_2 G: 34.15 kg/(m^2 s) T_{in}: 280 °C P: 2.5 MPa	Water G: 74.49 kg/(m^2 s) T_{in}: 108 °C P: 7.4 MPa	Numerical simulationv Flow-velocity profile Pressure drop Heat transfer rate
Zhang et al. [97]	Alloy 617 Counter-current flow	θ: 10–60° w_f: 0.8 mm l_f: 4–16 mm d_c: 0.94 mm	θ: 10–60° w_f: 0.8 mm l_f: 4–16 mm d_c: 0.94 mm	CO_2 Re: 20000 T_{in}: 875 K P: 15 MPa	CO_2 Re: 20000 T_{in}: 675 K P: 15 MPa	Numerical simulation Pressure drop Heat transfer coefficient

where $l_R = p_f/\cos\theta$ is the relative length. These friction factor correlations are valid for $50 \le Re \le 2000$, $5 < \theta < 45°$, $4.09 \le l_R/D \le 32.73$. For the above correlations, the unit of zigzag angle (θ) in the correlations is in radians.

4.3. PCHE with S-shaped fins

A summary of studies on the thermohydraulic performance of PCHEs with S-shaped fins is shown in Table 5 in chronological order.

In 2005, researchers from Tokyo Institute of Technology developed a PCHE with S-shape discontinuous fins and tested its thermohydraulic parameters using supercritical CO_2. Tsuzuki et al. [92,93] carried out supercritical CO_2 turbulence CFD studies with an RNG k-ε model to investigate the thermohydraulic performance of PCHE with S-shaped fins. They considered different fin shapes and angles, assuming that the supercritical CO_2 was in local equilibrium for thermodynamic and transport properties [98]. Results showed that the fin angle greatly affected the pressure drop but it did not significantly affect the heat transfer performance. Using the relationship of heat transfer rates per unit volume against the pressure drop per unit length, they obtained an optimal flow channel configuration that had only one-fifth of the pressure drop of the conventional zigzag configuration with equal heat transfer performance. Ngo et al. [60,74] manufactured a PCHE with S-shaped fins and carried out tests in a supercritical CO_2 test loop to confirm its performance. A conventional PCHE with zigzag fins was also designed for comparison, which had the same free flow area, hydraulic diameter, and fin angle. Experimental results showed that the pressure drop factor of the PCHE with S-shaped fins was 4–5 times lower and the Nusselt number 24–34% lower than those of the zigzag fins, depending on the Reynold number, as shown in Fig. 13. Based on the experimental results, Nusselt number and Fanning factor empirical correlations were developed as follows:

$$Nu = (0.1740 \pm 0.0118)Re^{(0.593\pm0.007)}Pr^{(0.430\pm0.014)} \text{ for } 3.5 \times 10^3 < Re < 2.3 \times 10^4,\ \ 0.75 < Pr < 2.2 \tag{38}$$

$$f = (0.4545 \pm 0.0405)Re^{(-0.340\pm0.009)} \text{ for } 3.5 \times 10^3 < Re < 2.3 \times 10^4,\ \ 0.75 < Pr < 2.2 \tag{39}$$

The calculation of Re was based on the channel hydraulic diameter. As shown in Fig. 14, these empirical correlations can predict the overall heat transfer coefficient and pressure drop well, with a standard deviation of ± 2.3% and ± 16.6%, respectively. Ngo et al. [94] determined the optimal fin and plate configuration for a PCHE with S-shaped fins using 3D CFD simulation and evaluated the thermohydraulic performance of the heat exchanger in a residential heat pump application [99]. Comparison with a conventional heat exchanger, the PCHE showed 3.3 times higher compactness, 37% lower pressure drop on the CO_2 side and ten times smaller volume on the water side. Comparison between experimental and numerical results of the performance of the PCHE showed a deviation of < 5% [100,101]. Tsuzuki et al. [95] used the validated RNG k-ε turbulence model for the development of supercritical CO_2 correlations around the pseudocritical point, where fluid properties change radically. Simulations with 20 different temperatures were performed with the fluid inlet temperature set 2 K lower or higher than the constant wall temperature for the cold and hot sides respectively. Based on the numerical results, Nusselt number correlations were developed for the cold (water)/hot (CO_2) sides:

$$Nu_{hot} = 0.207Re^{0.627}Pr^{0.340} \text{ for } 1.5 \times 10^3 < Re < 1.5 \times 10^4,\ \ 1 < Pr < 3 \tag{40}$$

$$Nu_{cold} = 0.253Re^{0.597}Pr^{0.349} \text{ for } 100 < Re < 1.5 \times 10^3,\ \ 2 < Pr < 11 \tag{41}$$

The deviations of the correlations were 1.47% for the water side and 0.90% for the CO_2 side. It should be noted that equations 38–41 were based on a single PCHE and thus only apply to PCHEs with similar geometric parameters. To further investigate the S-shaped fin effects, Tsuzuki et al. [96] conducted numerical parametric surveys with an RNG k-ε turbulence model to elucidate how the fin shape affects the thermohydraulic performance. The studied fin parameters including fin angle, overlapping length, fin width, fin length, and edge roundness. Fin angle proved to be the most effective parameter, a narrower fin can produce more heat transfer area per unit volume, but has worse fin efficiency than wider fins, while a longer fin can reduce the pressure drop that occurs due to the stream bend. Fin roundness at the head and tail edge of the fins has only minimal effect on heat transfer performance but greatly affects pressure drop. Methods to reduce pressure drop always lead to heat transfer deterioration and therefore, optimization parameters should be carefully selected considering thermohydraulic performance and manufacturing costs.

Following the work of Tsuzuki et al. [96], Zhang et al. [97] from the Ohio State University used multi-objective evolutionary algorithms for S-shaped fin optimization based on CFD simulations of nine S-shaped fin channel design models to maximize the heat exchanger thermal effectiveness and to minimize the overall pressure drop across the heat exchanger core. The selected shape factors for the S-shaped fin channel optimization were the fin angle and fin length and the objective functions were selected to be the heat transfer effectiveness and the pressure drop across the core. The optimization results indicated that the small-fin-angle channels with large fin length were able to reduce the pressure drop, while the large-fin-angle channels with small fin length were favourable in increasing the heat exchanger thermal effectiveness. They recommended the use of an S-shaped fin channel with 11.6° fin angle and 6.08 mm fin length for low pressure drop applications and 60° fin

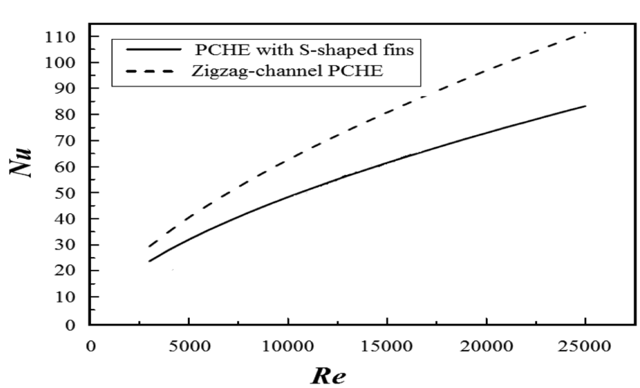

(a)

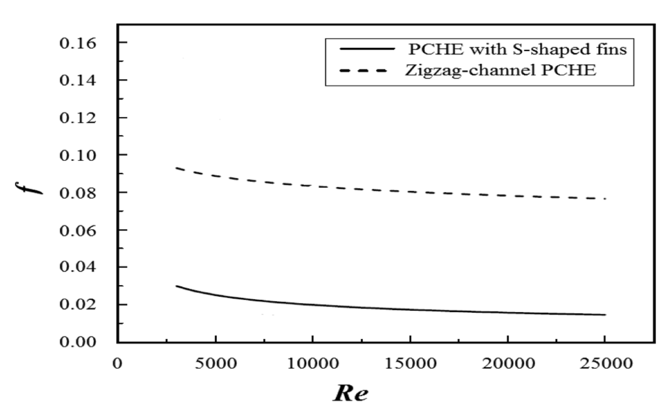

(b)

Fig. 13. Comparison between a PCHE with S-shaped fins and the zigzag-channel PCHE with the same free flow area, hydraulic diameter, and fin angle (a) Nusselt number, and (b) Fanning factor [60].

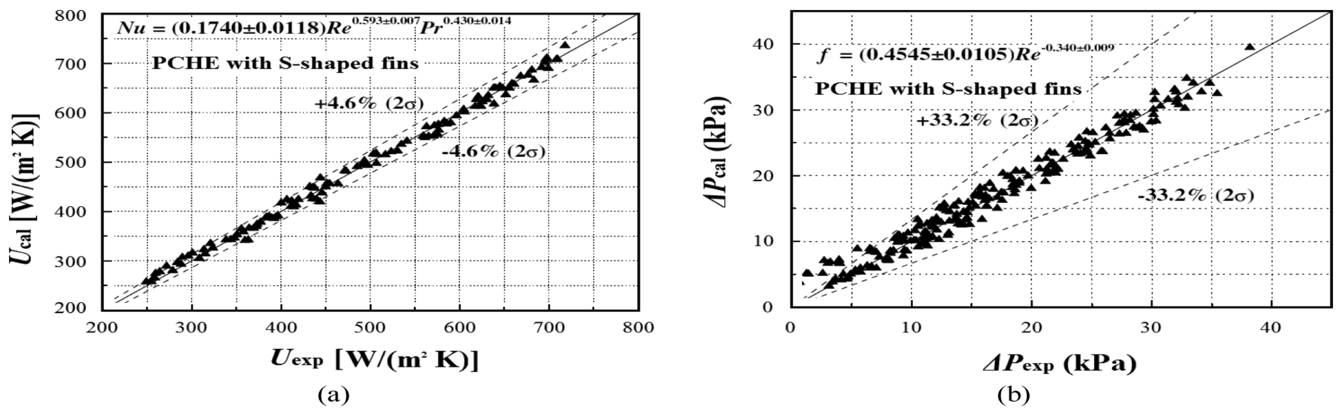

Fig. 14. Comparison of results obtained from proposed correlations and experiments for a PCHE with S-shaped fins (a) overall heat transfer coefficient, and (b) pressure drop [60].

angle and 9.95 mm fin length for medium pressure drop and high heat transfer effectiveness applications.

4.4. PCHE with airfoil fins

A summary of studies on the thermohydraulic performance of PCHEs with airfoil fins is shown in Table 6 in chronological order.

In 2008, researchers from Pohang University of Science and Technology first proposed a PCHE model with several airfoil shape fins (NACA 0020 model). Kim et al. [75] numerically investigated the thermohydraulic performance of PCHE with airfoil fins compared with the continuous zigzag configuration. The results showed that the PCHE

Table 6
Representative thermohydraulic performance studies of PCHEs with airfoil fins.

Reference	Test section description			Test conditions		Measured characteristics
	Typical description	Hot-side configuration	Cold-side configuration	Hot side	Cold side	
Kim et al. [75]	NACA 0020 airfoil Dimensions of 108 × 14.25 × 4.89 mm^3 Counter-current flow	p_f: 1–4 mm g_f: 3.34 mm w_f: 0.8 mm l_f: 4 mm n: 2	p_f: 1–4 mm g_f: 3.34 mm w_f: 0.8 mm l_f: 4 mm n: 1	CO_2 $\dot{m}$: 0.0001445 kg/s T_{in}: 279.9 °C P_{out}: 2.52 MPa	CO_2 $\dot{m}$: 0.0003152 kg/s T_{in}: 107.9 °C P_{out}: 8.28 MPa	Numerical simulation Flow-velocity profile Pressure drop Heat transfer rate
Yoon et al. [102]	NACA 0020 airfoil Alloy 800HT Counter-current flow	p_f: 1–4 mm g_f: 3.34 mm w_f: 0.8 mm l_f: 4 mm n: 2	p_f: 1–4 mm g_f: 3.34 mm w_f: 0.8 mm l_f: 4 mm n: 1	He and CO_2	CO_2	Numerical simulation Pressure factor Nusselt number
Xu et al. [103]	NACA 0025 airfoil Constant temperature boundary condition (60 °C)		p_f: 2 mm l_v: 1–3.5 mm w_f: 1 mm l_f: 4 mm d_c: 1 mm		CO_2 Re: 5007–125175 T_{in}: 30 °C	Numerical simulation Flow-velocity profile Pressure drop Nusselt number
Xu et al. [104]	Four different fins. Constant temperature boundary condition (60 °C)		p_f: 2 mm l_v: 1–3.5 mm w_f: 1 mm l_f: 4 mm d_c: 1 mm		CO_2 Re: 5007–125175 T_{in}: 30 °C	Numerical simulation Flow-velocity profile Pressure drop Nusselt number
Ma et al. [105]	NACA 0021 airfoil Alloy 617 6.72 × 2 × 6 mm^3 Counter-current flow	p_f: 6.5 mm l_v: 2 mm w_f: 0.84 mm l_f: 4 mm h_f: 1 mm	p_f: 6.5 mm l_v: 2 mm w_f: 0.84 mm l_f: 4 mm h_f: 1 mm	Helium Re: 2287–5145 T_{in}: 1173.15 K P_{out}: 7.59 MPa	Helium Re: 2287–5145 T_{in}: 761.96 K P_{out}: 7.83 MPa	Numerical simulation Flow-velocity profile Temperature profile Pressure factor Nusselt number
Kim et al. [106]	NACA 0020 airfoil Counter-current flow	p_f: 6–10.5 mm l_v: 1.6–2.8 mm w_f: 0.8 mm l_f: 6 mm d_c: 0.8 mm	p_f: 6–10.5 mm l_v: 1.6–2.8 mm w_f: 0.8 mm l_f: 6 mm d_c: 0.8 mm	CO_2 $\dot{m}$: 0.4–4.8 g/s T_{in}: 451.3 °C T_{out}: 240 °C P_{in}: 7.75 MPa P_{out}: 7.68 MPa	CO_2 $\dot{m}$: 0.4–4.8 g/s T_{in}: 216.1 °C T_{out}: 409 °C P_{in}: 19.8 MPa P_{out}: 19.7 MPa	Numerical simulation Pressure factor Nusselt number Euler number Heat transfer rate
Kwon et al. [107]	NACA 0020 airfoil Counter-current flow	p_f: 6–10.5 mm l_v: 1.6–2.8 mm w_f: 0.8 mm l_f: 6 mm d_c: 0.8 mm	p_f: 6–10.5 mm l_v: 1.6–2.8 mm w_f: 0.8 mm l_f: 6 mm d_c: 0.8 mm	CO_2 $\dot{m}$: 0.6–6 g/s T_{in}: 618 K P_{in}: 7.715 MPa	CO_2 $\dot{m}$: 0.6–6 g/s T_{in}: 585 K P_{in}: 19.7 MPa	Numerical simulation Pressure factor Nusselt number
Chu et al. [108]	NACA 0025 airfoil Constant temperature boundary condition (120 °C)		p_f: 0–8 mm l_v: 2–4 mm w_f: 1 mm l_f: 4 mm d_c: 1 mm	120 °C	CO_2 $\dot{m}$: 1–5 g/s P_{in}: 0.8 MPa	Numerical simulation Pressure factor Nusselt number

with airfoil fins can achieve the same heat transfer performance with a pressure drop only one-twentieth that of a zigzag-channel PCHE. They attributed the equal heat transfer performance to the enhancement of the heat transfer area and the uniform flow configuration, while the reduction of pressure drop was due to the suppression of the generation of separated flow, owing to the streamlined shape. Kim et al. [106] performed sensitivity analysis with various design parameters to configure the optimal arrangement of airfoil fins by using CFD analysis for a supercritical CO_2 system. Three geometric parameters, staggered pitch, horizontal pitch and vertical pitch were considered for the optimization of the airfoil fin design, and the effects of the Reynolds number, Nusselt number and Euler number were considered for optimization. The objective function to optimize the arrangement was selected as the ratio of Nusselt number to Euler number, *Nu/Eu*. Results showed that the fully staggered arrangement ($2p_f/l_h$) had the best performance, considering both heat transfer and pressure drop. Euler number was found to increase and Nusselt number decreased as the horizontal number (l_h/l_f) increased. The opposite trend was seen for the vertical number (l_v/w_f). For horizontal and vertical numbers greater than 2, there was no enhancement of the heat transfer at the fin. Kim et al. [75] and Yoon et al. [102] from the Korea Advanced Institute of Science & Technology developed a k-ε model with enhanced wall treatment for 3D turbulent flow analysis for Reynolds numbers up to 1.5×10^5 in order to develop thermohydraulic correlations for PCHE with airfoil fins. He, CO_2, Na, and Alloy 800HT were used for the simulations with fluid properties obtained from the NIST chemistry webbook. Based on the CFD results, the following correlations were developed for the Nusselt number and Fanning friction factor:

$$Nu = 3.7 + 0.0013Re_{min}^{1.12}Pr^{0.38} \text{ for } 0 < Re_{min} < 2500,\ \ 0.6 < Pr < 0.8 \tag{42}$$

$$Nu = 0.027Re_{min}^{0.78}Pr^{0.4} \text{ for } 3 \times 10^3 < Re_{min} < 1.5 \times 10^5,\ \ 0.6 < Pr < 0.8 \tag{43}$$

$$fRe_{min} = 9.31 + 0.028Re_{min}^{0.86} \text{ for } 0 < Re_{min} < 1.5 \times 10^5 \tag{44}$$

where Re_{min} is the Reynolds number at the minimum flow area and the calculations of *Nu* and *Re* are based on the channel hydraulic diameter. These three equations were developed for a specific PCHE and thus only applied to the geometry investigated.

As mentioned earlier, airfoil fins can have improved thermohydraulic performance over zigzag fins when applied to PCHE with supercritical CO_2 as the working fluid. To further improve the thermohydraulic performance of PCHEs, researchers from Xi'an Jiaotong University in China focused on optimization and novel airfoil fin shapes. Xu et al. [103,104] numerically investigated the effects of airfoil fin arrangements on heat transfer and flow resistance with SST k-ε model and constant temperature boundary condition (60 °C) for the top wall, bottom wall and fins. Comparison of parallel and staggered arrangements showed that the difference in Nusselt numbers between the two arrangements were quite small. However, the pressure drop per unit length in the staggered arrangement was much smaller than that of the parallel arrangement, concluding that staggered fin arrangement leads to better thermohydraulic performance compared to parallel fin arrangement. To further reduce the flow resistance, they recommended a sparse arrangement of fins and modified the head of the airfoil fin to be swordfish shape, as shown in Fig. 15. Ma et al. [105] investigated the manufacture of airfoil PCHE plate and the effect of the fillets formed on the end walls of airfoil fin during the photochemical etching process. They found that the fin end-wall fillet can increase the heat transfer and pressure drop because of small vortices formed at the leading and trailing edges of the fins. Chu et al. [108] investigated the geometrical parameters of airfoil fins (fin length, fin width, transverse pitch and longitudinal pitch) on the thermohydraulic performance of PCHE. Local thermohydraulic results showed that the heat transfer rate decreases due to the strong variation in the properties of supercritical CO_2, but that the pressure loss remained almost constant along the main flow direction. Study of the pitch parameters indicated that a parallel distribution of airfoil fin can enhance the heat transfer with higher flow resistance, while a staggered distribution can improve the comprehensive heat transfer performance. Based on the numerical results, the Colburn factor and Darcy friction factor correlations of PCHE with distributed airfoil fins were fitted as follows:

$$j = 0.026\left(\frac{p_f}{l_f}\right)^{-0.170}\left(\frac{w_f}{l_v}\right)^{-0.248}Re_{in}^{-0.19\times\left(\frac{w_f}{l_v}\right)^{-0.187}} \quad \text{for } 8 \times 10^3 < Re < 10^5 \tag{45}$$

$$f = 0.357\left(\frac{p_f}{l_f}\right)^{-0.252}\left(\frac{w_f}{l_v}\right)^{-0.255}Re_{in}^{-0.173\times\left(\frac{w_f}{l_v}\right)^{-0.274}} \quad \text{for } 8 \times 10^3 < Re < 10^5 \tag{46}$$

where Re_{in} is the inlet Reynolds number. These correlations can predict the numerical results with a maximal error of < 5% within the range of applied Reynolds number. It can be found that these two correlations are independent of *Pr*, which make them be only applied to the same operating conditions as Chu et al. [108].

5. Optimisation

Heat exchanger optimization is an important field, full of challenges, involving many different optimization criteria. For supercritical CO_2 power cycles, heat exchanger design optimization is particularly important due to their high capital and operating costs [109]. In recent years, many researchers have undertaken significant work on the optimization of PCHE devices.

Lee and Kim [83] defined an objective function for the Euler number and the effectiveness of the heat exchanger for a geometric design of zigzag channel PCHE. The function included the ratio of the radius of the fillet to the hydraulic diameter of the channels, the ratio of wavelength to the hydraulic diameter of the channels, and the ratio of wave height to the hydraulic diameter of the channels. Following this, they updated their optimization method to a multi-objective genetic algorithm to find the Pareto optimal front [80]. This method employed two non-dimensional objective functions related to heat transfer performance and friction losses for a geometric design, including the cold channel angle and the ellipse aspect ratio of the cold channel. Kim et al. [106] suggested an objective function of Nusselt number to Euler number for the optimization design of PCHE with airfoil shaped fins, including staggered pitch, horizontal pitch and vertical pitch. Based on their objective functions, they obtained some optimal geometric designs for PCHE. Rajabifar et al. [110,111] and Chai et al. [112] also recommended the use of the ratio of Nusselt number to Euler number as

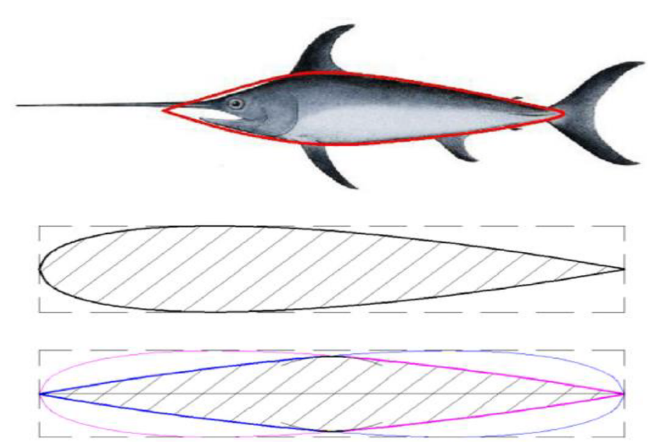

Fig. 15. Motivation of optimization for PCHE with airfoil fins [103].

the objective function for the optimisation process. However, they did not present evidence of defined weighting of their objective function, assigning the same weight to heat transfer and pressure drop even though each made a different contribution to the overall performance of the heat exchanger, as pointed out by Kwon et al. [107]. Considering the convenience of the objective function for optimization design of PCHE and also the different contribution of heat transfer and pressure drop, Guo and Huai [113,114] employed the entropy generation rate of heat transfer and pressure drop to inform PCHE selection for a supercritical CO_2 Brayton cycle. The local entropy generation rates caused by irreversibilities in heat transfer and pressure drop, were defined as [115]:

$$S_{g,T} = \int_{i}^{o} \left(\frac{\dot{m} c_p dT}{T}\right)_{h,c} = \dot{m}_h c_{p,h} \ln\left(\frac{T_{h,o}}{T_{h,i}}\right) + \dot{m}_c c_{p,h} \ln\left(\frac{T_{c,o}}{T_{c,i}}\right) \tag{47}$$

$$S_{g,p} = \int_{i}^{o} \left(\frac{\dot{m} R_g dp}{p}\right)_{h,c} = \dot{m}_h R_g \ln\left(\frac{p_{h,o}}{p_{h,i}}\right) + \dot{m}_c R_g \ln\left(\frac{p_{c,o}}{p_{c,i}}\right) \tag{48}$$

where R_g is the ideal gas constant for CO_2. The local entropy generation rates were then integrated to determine the total entropy generation rate which was used as the objective function to study the influence of constraints such as mass flow rate, total length of heat transfer channel, thickness of the cold plate and the thermal conductivity of the plate on the overall performance of the PCHE.

Facing the challenge of optimal design of PCHE, some researchers introduced the cost-based objective functions which gave reasonable weighting to heat transfer and pressure drop. Kim and No [78] employed the sum of the capital cost and operating cost as the objective function for optimization of the design of a zigzag-channel PCHE. Yoon et al. [102] used the objective functions of the total cost with the operating condition to compare straight channel, zigzag channel, S shape and airfoil fin PCHEs. Kwon et al. [107] also suggested the use of a cost-based objective function for optimization of PCHE for the recuperator of a small-scale Brayton cycle. However, the problem of the cost-based objective function is that the capital cost and operating cost change significantly depending on the application and it is difficult to evaluate the accurate heat transfer and pressure drop contributions to the overall performance of the heat exchanger because of the uncertainties in empirical correlations.

PCHE is also a type of microchannel heat exchanger, and the zigzag configuration, S-shaped fins, and airfoil fins can be thought as passive methods for heat transfer enhancement. Therefore, the optimization used for microchannel heat exchanger with passive structures can be suitable for PCHE. Several experimental, numerical and theoretical studies have been carried out for the optimal design, and the optimization usually imposes severe constraints on the heat exchanger and system design for a given heat transfer rate. These constraints included the mass flow rate, pressure drop, fluid temperature rise, and temperature difference between fluid inlet and surface [116]. The optimal design methods are usually based on a given thermal resistance or a given pumping power or a given fluid flow rate. Singhal and Garimella [117,118], Gosselin and Bejan [119], and Canhoto and Reis [120] performed optimization methods based on the minimization of pumping power requirement to evaluate the heat transfer performance for a given thermal resistance. Tsai and Reiyu [121] and Liu and Garimella [122] established theoretical optimization models based on thermal resistance minimization to predict microchannel heat exchanger performance for a given pumping power. Promvonge et al. [123], Xia et al. [124,125], Chai et al. [126,127], and Zhang et al. [128] used the performance evaluation criteria to comprehensively access the heat exchanger for a given pumping power. The performance evaluation criterion (η) is defined as the ratio of the heat transfer coefficient of the optimal geometry to that of the reference at an equal pumping power by Webb [129] ,

$$\eta = \left.\frac{h_{opt}}{h_{ref}}\right|_{PP} = \left.\frac{Nu_{opt}}{Nu_{ref}}\right|_{PP} = \frac{Nu_{opt}/Nu_{ref}}{(f_{opt}/f_{ref})^{1/3}} \tag{49}$$

where Nu_{ref} and f_{ref} stand for Nusselt number and friction factor of the reference, respectively. Khan et al. [130], Famouri et al. [131], Shi and Dong [132], Zhai et al. [133], and Chai et al. [127] developed optimization methods based on entropy generation minimization proposed by Bejan [115] to study the optimization of thermal and hydraulic resistances for a given fluid flow rate or a Reynolds number.

In addition to the optimization methods mentioned above, some

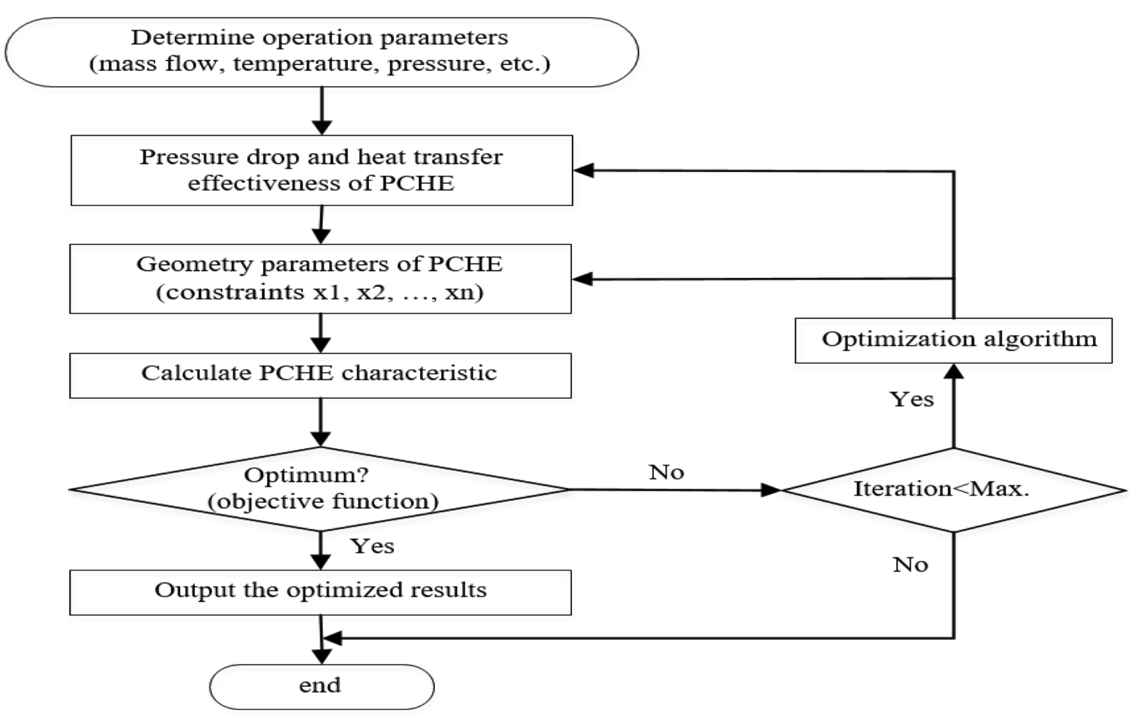

Fig. 16. General flowchart of optimization procedure for PCHE.

interesting work has been done using genetic algorithms for optimization design of compact heat exchangers. Xie et al. [134] applied a generalized procedure based on *ε-NTU* and the genetic algorithm technique for the optimization of a plate-fin compact heat exchanger. The minimum total volume and total annual cost of the heat exchanger were taken as objective functions and the geometries of the fins were fixed while three shape parameters were varied for the optimization objectives, with or without pressure drop constraints. They concluded that the genetic algorithm could provide a strong auto-search and combined optimization capability in the design of heat exchangers. Mishra et al. [135] proposed a genetic-algorithm based optimization technique for crossflow plate-fin heat exchangers using offset-strip fins. The optimization programme minimized the number of entropy generation units for a specific heat duty under given footprint constraint. Their results demonstrated the application and importance of a design approach based on the second law of thermodynamics as well as the suitability of the genetic algorithm for optimization of complex heat exchangers. However, they also suggested that the optimum design was highly sensitive to some of the geometric parameters and that a small deviation from the optimum value may give a large degradation in performance. Bacellar et al. [136] presented a multi-objective genetic algorithm along with a segmented *ε-NTU* approach method for a multi-scale analysis with topology and shape optimization for a full-scale heat exchanger design. The objective function was the entropy generation index ($\psi = \frac{NTU}{N_S} = \frac{UA}{\dot{S}_{gen}}$) from Ogiso [137], and the total fluid pumping power was used as a direct measure of the energy cost to deliver the objective function. They tested how the entropy generation varied with the different surfaces and how it affected the overall performance and obtained an optimally designed heat exchanger, which had a potential size reduction of more than 50%, with a similar reduction in pumping power compared to the baseline microchannel heat exchanger. The general flowchart of the optimization procedure for PCHE is shown in Fig. 16 and the general flowchart of the genetic algorithm is shown in Fig. 17.

6. Conclusions

Printed Circuit Heat Exchangers (PCHEs) extend the applications of compact heat exchangers where pressure, temperature or corrosion prevent the use of conventional heat exchangers. The all-welded construction of PCHEs manufactured from high-strength and corrosion-resistant alloys makes them suitable for very high-temperature and high-pressure applications, while their highly compact construction and exceptionally high heat transfer coefficients make them a good choice for demanding thermal energy transfer applications. This paper provides a comprehensive review of PCHEs, covering material selection, manufacturing and assembly, types of flow passages, thermohydraulic performance, heat transfer and pressure drop correlations, as well as geometric design optimisation methods. The paper provides a good review of state of the art and identifies gaps for further research and development.

The main summary of the review is as follows: (i) PCHEs relate to high-strength, high-temperature materials. At operating temperatures lower than 650 °C, 316/316L/347 stainless steel can be employed for the manufacture of PCHEs whereas for operating temperatures higher than 650 °C, nickel-based alloys, such as Alloy 625 or 617, can safely be employed but at much higher capital cost. (ii) Creep and corrosion are the two most important factors influencing material selection, but very little experimental data is available for helium or supercritical CO_2 in high-temperature environments. (iii) Photochemical machining and diffusion bonding are the two main processes of PCHE manufacture. Photochemical machining provides flexibility in thermohydraulic design, and diffusion bonding forms a compact, strong, all-metal heat exchanger core. (iv) Four main types of PCHE flow passages that

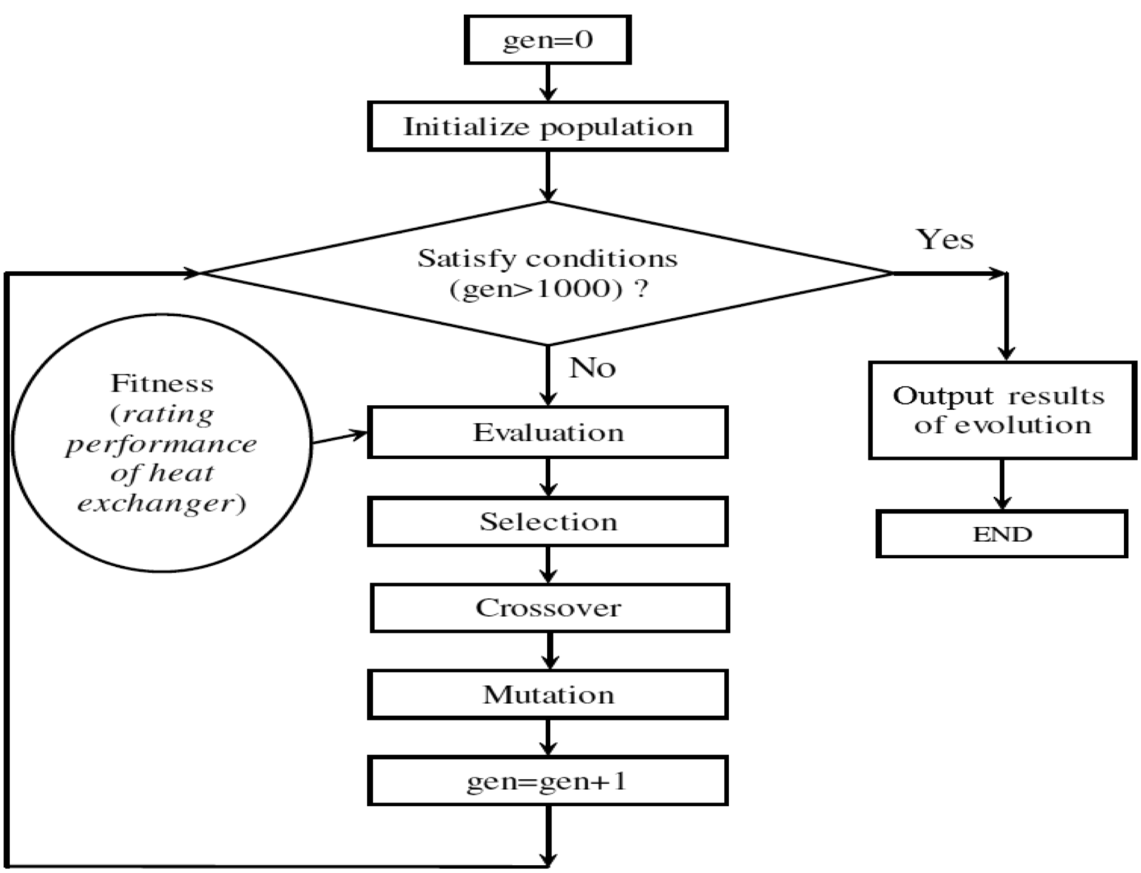

Fig. 17. General flowchart of genetic algorithm [136].

include: straight channel; zigzag (or wavy) channel; channel with S-shaped fins; and channel with airfoil fins, have been developed and tested at test facilities in the USA, Japan, Korea and China using helium and supercritical CO_2 as the working fluids. Their thermohydraulic performance has been investigated both experimentally and numerically. The test conditions for helium were 900 ˚C and 3.0 MPa, while for supercritical CO_2 test conditions were 500 ˚C and 20 MPa. Generally, PCHEs with airfoil fins showed best performance, followed by S-shaped fins and zigzag (or wavy) channel PCHEs. (v) Several authors have developed empirical correlations for the prediction of average heat transfer and pressure drop characteristics. However, most of the correlations were developed for a specific flow passage and using thermophysical properties corresponding to the average temperature and pressure at inlet and outlet conditions. (vi) Several optimization techniques for PCHE design have also been developed, usually based on the relationship between the Euler and Nusselt numbers and the cost-based objective function consisting of the capital cost of the PCHE and operating costs by assigning relative weighting factors to heat transfer and pressure drop for different operating conditions.

Recommendations for further work to fill knowledge gaps include:

a) Refinement of the composition of materials to improve mechanical properties and corrosion resistance for both helium and supercritical CO_2 for operation at temperatures and pressures, above 650 ˚C and 200 bar respectively.
b) Further optimisation of the geometry of PCHEs to simplify the design without compromising performance, in order to reduce the number and complexity of the fabrication steps and overall cost of manufacture.
c) More experimental and numerical studies are required to enable accurate local heat transfer and pressure drop data to be obtained for the development of more universal correlations that are able to cover a wide range of geometry and flow parameters to facilitate the design and performance prediction of PCHEs.

Declaration of Competing Interest

The authors declare that they have no known competing financial interests or personal relationships that could have appeared to influence the work reported in this paper.

Acknowledgements

The work presented in this paper is supported by a number of funders as follows: i) The UK Engineering and Physical Sciences Research Council (EPSRC) under research grants EP/P004636/1 ‘Optimising Energy Management in Industry – OPTEMIN’, and EP/K011820/1 (Centre for Sustainable Energy Use in Food Chains) and ii) the European Union’s Horizon 2020 research and innovation programme and funding for project I-ThERM (Industrial Thermal Energy Recovery and Management) under grant agreement No. 680599. The authors would also like to acknowledge the financial support and inputs made by a number of industry partners and collaborators. All data used are in the paper but if any additional information is required it can be obtained by contacting the corresponding author.

References

[1] DoE U S. A technology roadmap for generation IV nuclear energy systems. Nuclear Energy Research Advisory Committee and the Generation IV International Forum, 2002, pp. 48-52.
[2] P. Sabharwall, E.S. Kim, M. McKellar et al. Process heat exchanger options for the advanced high temperature reactor Idaho National Laboratory (INL), 2011.
[3] R.K. Shah, D.P. Sekulic, Fundamentals of heat exchanger design, John Wiley & Sons, 2003.
[4] W. Chu, X. Li, T. Ma, et al., Experimental investigation on SCO_2-water heat transfer characteristics in a printed circuit heat exchanger with straight channels, Int. J. Heat Mass Transf. 113 (2017) 184–194.
[5] V. Dostal, P. Hejzlar, M.J. Driscoll, High-performance supercritical carbon dioxide cycle for next-generation nuclear reactors, Nucl. Technol. 154 (3) (2006) 265–282.
[6] V. Dostal, M.J. Driscoll, P. Hejzlar et al. Supercritical CO2 cycle for fast gas-cooled reactors. ASME Paper No. GT2004-54242, 2004.
[7] Y.J. Baik, S. Jeon, B. Kim, et al., Heat transfer performance of wavy-channeled PCHEs and the effects of waviness factors, Int. J. Heat Mass Transf. 114 (2017) 809–815.
[8] B. Halimi, K.Y. Suh, Computational analysis of supercritical CO_2 Brayton cycle power conversion system for fusion reactor, Energy Convers. Manage. 63 (2012) 38–43.
[9] L. Chen, X.R. Zhang, Experimental analysis on a novel solar collector system achieved by supercritical CO_2 natural convection, Energy Convers. Manage. 77 (2014) 173–182.
[10] J.W. Seo, Y.H. Kim, D. Kim, et al., Heat transfer and pressure drop characteristics in straight microchannel of printed circuit heat exchangers, Entropy 17 (5) (2015) 3438–3457.
[11] B.S. Haynes, A.M. Johnston, High-effectiveness micro-exchanger performance. AIChE 2002 Spring National Meeting, 2002.
[12] L.M. Pua, S.O. Rumbold, Industrial microchannel devices-where are we today? First Int. Conf. Microchannels Minichannels (2003) 773–780.
[13] Y. Fan, L. Luo, Recent applications of advances in microchannel heat exchangers and multi-scale design optimization, Heat Transfer Eng. 29 (5) (2008) 461–474.
[14] D.M. Allen, Photochemical machining: from ‘manufacturing's best kept secret’ to a $6 billion per annum, rapid manufacturing process CIRP Annals-Manufacturing Technology, 53 (2) 2004, 559–572.
[15] S. Ashman, S.G. Kandlikar, A review of manufacturing processes for microchannel heat exchanger fabrication Proc. Fourth International Conference on Nanochannels, Microchannels and Minichannels, 2006, 19–21.
[16] Video & Photo Gallery. http://www.vpei.com/diffusion-bonded-microchannel-heat-exchangers/.
[17] Y. Ahn, S.J. Bae, M. Kim, et al., Review of supercritical CO_2 power cycle technology and current status of research and development, Nucl. Eng. Technol. 47 (6) (2015) 647–661.
[18] L. Cheng, G. Ribatski, J.R. Thome, Analysis of supercritical CO_2 cooling in macro- and micro-channels, Int. J. Refrig. 31 (8) (2008) 1301–1316.
[19] L.F. Cabeza, A. de Gracia, A.I. Fernández, et al., Supercritical CO_2 as heat transfer fluid: A review, Appl. Therm. Eng. 125 (2017) 799–810.
[20] C. Huang, W. Cai, Y. Wang, et al., Review on the characteristics of flow and heat transfer in printed circuit heat exchangers, Appl. Therm. Eng. 153 (2019) 190–205.
[21] S.A. Wright, T.M. Conboy, E.J. Parma, et al. Summary of the Sandia Supercritical CO2 Development Program Sandia National Laboratories (SNL-NM), Albuquerque, NM (United States), 2011.
[22] D.D. Fleming, A.M. Kruizenga Identified corrosion and erosion mechanisms in SCO2 Brayton Cycles. Sandia National Laboratories (SNL-NM), Albuquerque, NM (United States); Sandia National Laboratories, Livermore, CA, 2014.
[23] B. Sunden, High temperature heat exchangers (HTHE), Technology, VIT University, Vellore, India, 2005.
[24] B.A. Pint, K.L. More, P.F. Tortorelli, The Effect of Water Vapor on Oxidation Performance of Alloys Used in Recuperators. ASME Paper No. GT-2002-30543, 2002.
[25] D.J. Zhang, M. Zeng, J.W. Wang, et al., Creep analysis of cross wavy primary surface recuperator for microturbine system, Proceed. ASME Turbo Expo. 2008 (1) (2008) 899–904.
[26] P.J. Maziasz, R.W. Swindeman, Selecting and developing advanced alloys for creep-resistance for microturbine recuperator applications, J. Eng. Gas Turbines Power 125 (1) (2003) 310–315.
[27] P.J. Maziasz, B.A. Pint, R.W. Swindeman, et al. Selection, Development and Testing of Stainless Steels and Alloys for High-Temperature Recuperator Applications. ASME Paper No. GT2003-38762, 2003.
[28] P.J. Maziasz, B.A. Pint, J.P. Shingledecker, et al., Advanced alloys for compact, high-efficiency, high-temperature heat-exchangers, Int. J. Hydrogen Energy 32 (16) (2007) 3622–3630.
[29] P.J. Maziasz, J.P. Shingledecker, B.A. Pint, et al., Overview of creep strength and oxidation of heat-resistant alloy sheets and foils for compact heat exchangers, J. Turbomach. 128 (4) (2006) 814–819.
[30] H. Osman, A. Borhana, M.N. Tamin, Material parameters for creep rupture of austenitic stainless steel foils, J. Mater. Eng. Perform. 23 (8) (2014) 2858–2863.
[31] N.D. Evans, P.J. Maziasz, J.P. Shingledecker, et al., Microstructure evolution of alloy 625 foil and sheet during creep at 750 °C, Mater. Sci. Eng., A 498 (1) (2008) 412–420.
[32] X. Li, D. Kininmont, R. Le Pierres, et al. Alloy 617 for the high temperature diffusion-bonded compact heat exchangers. Proceedings of ICAPP08, Anaheim, CA, Paper, 2008, 8008.
[33] J. Klöwer, R.U. Husemann, M. Bader, Development of nickel alloys based on alloy 617 for components in 700 ˚C power plants, Procedia Eng. 55 (2013) 226–231.
[34] J.K. Wright, R.N. Wright, N.J. Lybeck, Progress Report on Alloy 617 Isochronous Stress-Strain Curves Idaho National Laboratory (INL), 2014.
[35] J.K. Wright, Progress Report on Alloy 617 Time Dependent Allowables Idaho National Laboratory (INL), Idaho Falls, ID (United States), 2015.
[36] K. Natesan, A. Moisseytsev, S. Majumdar, Preliminary issues associated with the next generation nuclear plant intermediate heat exchanger design, J. Nucl. Mater. 392 (2) (2009) 307–315.
[37] G.G. Lee, S. Jung, J.Y. Park, et al., Microstructural investigation of Alloy 617 creep-ruptured at high temperature in a helium environment, J. Mater. Sci.

Technol. 29 (12) (2013) 1177–1183.
[38] S.F. Di Martino, R.G. Faulkner, S.C. Hogg, et al., Characterisation of microstructure and creep properties of alloy 617 for high-temperature applications, Mater. Sci. Eng., A 619 (2014) 77–86.
[39] D. Kaoumi, K. Hrutkay, Tensile deformation behavior and microstructure evolution of Ni-based super alloy 617, J. Nucl. Mater. 454 (1) (2014) 265–273.
[40] W.G. Kim, J.Y. Park, I.M.W. Ekaputra, et al., Creep deformation and rupture behavior of Alloy 617, Eng. Fail. Anal. 58 (2015) 441–451.
[41] P. Rodriguez, Selection of materials for heat exchangers, Alexandria, Egypt, 1997.
[42] B.A. Pint, Stainless steels with improved oxidation resistance for recuperators, J. Eng. Gas Turbines Power 128 (2) (2006) 370–376.
[43] R.W. Swindeman, D.L. Marriott Criteria for design with structural materials in combined-cycle applications above 815 F. Transactions-American Society of Mechanical Engineers Journal of Engineering for Gas Turbines and Power, 1994, 116: 352-352.
[44] R.H. Kane, The evolution of high temperature alloys: a designer's perspective, Heat-Resistant Materials (1991) 1–8.
[45] M. Anderson, G. Nellis, M. Corradini, Materials, Turbomachinery and heat exchangers for supercritical CO_2 systems, Battelle Energy Alliance, LLC, 2012.
[46] K. Sridharan, M.H. Anderson, G. Cao et al. Corrosion testing of materials in high temperature supercritical carbon-dioxide environment. Proceedings of Supercritical CO2 Power Cycle Symposium, Boulder, CO. 2011.
[47] G. Cao, V. Firouzdor, K. Sridharan, et al., Corrosion of austenitic alloys in high temperature supercritical carbon dioxide, Corros. Sci. 60 (2012) 246–255.
[48] V. Firouzdor, K. Sridharan, G. Cao, et al., Corrosion of a stainless steel and nickel-based alloys in high temperature supercritical carbon dioxide environment, Corros. Sci. 69 (2013) 281–291.
[49] H.J. Lee, H. Kim, S.H. Kim, et al., Corrosion and carburization behavior of chromia-forming heat resistant alloys in a high-temperature supercritical-carbon dioxide environment, Corros. Sci. 99 (2015) 227–239.
[50] H.J. Lee, G.O. Subramanian, S.H. Kim, et al., Effect of pressure on the corrosion and carburization behavior of chromia-forming heat-resistant alloys in high-temperature carbon dioxide environments, Corros. Sci. 111 (2016) 649–658.
[51] F. Rouillard, F. Charton, G. Moine, Corrosion behavior of different metallic materials in supercritical carbon dioxide at 550 C and 250 bars. Corrosion, J. Sci. Eng. 67 (9) (2011) 095001-095001-7.
[52] G.R. Holcomb, C. Carney, Ö.N. Doğan, Oxidation of alloys for energy applications in supercritical CO_2 and H_2O, Corros. Sci. 109 (2016) 22–35.
[53] S. Sarrade, D. Féron, F. Rouillard, et al., Overview on corrosion in supercritical fluids, J. Supercrit. Fluids 120 (2017) 335–344.
[54] Compact Heat Exchangers a Training Package for Engineers. Energy Efficiency Office, London, UK, 2000.
[55] HEXCES Technical Brochure. http://www.hexces.com/technology.
[56] S.K. Mylavarapu, X. Sun, R.N. Christensen, Photofabrication and surface roughness of flow channels for a compact high-temperature heat exchanger, Trans. Am. Nucl. Soc. 99 (2008) 837–839.
[57] D. Southall. Diffusion bonding in compact heat exchangers. Proceedings of Supercritical CO2 Power Cycle Symposium, 2011, 24-25.
[58] S.K. Mylavarapu, X. Sun, R.N. Christensen, et al., On the diffusion bonding of Alloy 617 for high-temperature compact heat exchangers, Trans. Am. Nucl. Soc. 101 (2009) 370–372.
[59] P. Sabharwall, D.E. Clark, R.E. Mizia, et al., Diffusion-welded microchannel heat exchanger for industrial processes, J. Therm. Sci. Eng. Appl. 5 (1) (2013) 011009.
[60] T.L. Ngo, Y. Kato, K. Nikitin, et al., Heat transfer and pressure drop correlations of microchannel heat exchangers with S-shaped and zigzag fins for carbon dioxide cycles, Exp. Therm Fluid Sci. 32 (2) (2007) 560–570.
[61] S.K. Mylavarapu, X. Sun, R.N. Christensen, et al., Fabrication and design aspects of high-temperature compact diffusion bonded heat exchangers, Nucl. Eng. Des. 249 (2012) 49–56.
[62] S. Mylavarapu, X. Sun, J. Figley, et al., Investigation of high-temperature printed circuit heat exchangers for very high temperature reactors, J. Eng. Gas Turbines Power 131 (6) (2009) 062905.
[63] S.K. Mylavarapu, X. Sun, R.E. Glosup, et al., Thermal hydraulic performance testing of printed circuit heat exchangers in a high-temperature helium test facility, Appl. Therm. Eng. 65 (1) (2014) 605–614.
[64] J. Figley, X. Sun, S.K. Mylavarapu, et al., Numerical study on thermal hydraulic performance of a Printed Circuit Heat Exchanger, Prog. Nucl. Energy 68 (2013) 89–96.
[65] M. Chen, X. Sun, R.N. Christensen, et al., Experimental and numerical study of a printed circuit heat exchanger, Ann. Nucl. Energy 97 (2016) 221–231.
[66] A.M. Aneesh, A. Sharma, A. Srivastava, et al., Thermal-hydraulic characteristics and performance of 3D straight channel based printed circuit heat exchanger, Appl. Therm. Eng. 98 (2016) 474–482.
[67] W. Kim, Y.J. Baik, S. Jeon, et al., A mathematical correlation for predicting the thermal performance of cross, parallel, and counterflow PCHEs, Int. J. Heat Mass Transf. 106 (2017) 1294–1302.
[68] J.E. Hesselgreaves, R. Law, D. Reay, Compact heat exchangers: selection, design and operation, Butterworth-Heinemann, 2016.
[69] V. Gnielinski, New equations for heat and mass transfer in turbulent pipe and channel flow, Int. Chem. Eng. 16 (2) (1976) 359–368.
[70] J.P. Abraham, E.M. Sparrow, J.C.K. Tong, Heat transfer in all pipe flow regimes: laminar, transitional/intermittent, and turbulent, Int. J. Heat Mass Transf. 52 (3) (2009) 557–563.
[71] K. Nikitin, Y. Kato, L. Ngo Experimental and numerical study of printed circuit heat exchanger performance in carbon dioxide experimental loop. Proceedings of 6th Gustav Lorentzen Natural Working Fluids Conf., Glasgow, UK, August 29–September 1, 2004.
[72] T. Ishizuka. Thermal-hydraulic characteristics of a printed circuit heat exchanger in a supercritical CO2 Loop. The 11th International Topical Meeting on Nuclear Reactor Thermal-Hydraulics, 2005.
[73] K. Nikitin, Y. Kato, L. Ngo, Printed circuit heat exchanger thermal–hydraulic performance in supercritical CO_2 experimental loop, Int. J. Refrig 29 (5) (2006) 807–814.
[74] K. Nikitin, Y. Kato, T. Ishizuka Experimental thermal-hydraulics comparison of microchannel heat exchangers with zigzag channels and S-shaped fins for gas turbine reactors. Proc. of Fifteenth International Conference on Nuclear Engineering, Nagoya, Japan, April 22–26, (2007), ICONE15–10826.
[75] D.E. Kim, M.H. Kim, J.E. Cha, et al., Numerical investigation on thermal-hydraulic performance of new printed circuit heat exchanger model, Nucl. Eng. Des. 238 (12) (2008) 3269–3276.
[76] I.H. Kim, H.C. No, J.I. Lee, et al., Thermal hydraulic performance analysis of the printed circuit heat exchanger using a helium test facility and CFD simulations, Nucl. Eng. Des. 239 (11) (2009) 2399–2408.
[77] I.H. Kim, H.C. No, Thermal hydraulic performance analysis of a printed circuit heat exchanger using a helium-water test loop and numerical simulations, Appl. Therm. Eng. 31 (17) (2011) 4064–4073.
[78] I.H. Kim, H.C. No, Physical model development and optimal design of PCHE for intermediate heat exchangers in HTGRs, Nucl. Eng. Des. 243 (2012) 243–250.
[79] S.M. Lee, K.Y. Kim A parametric study on fluid flow and heat transfer in a printed circuit heat exchanger. Proceedings of the ASME/JSME 2011 8th Thermal Engineering Joint Conference (AJTEC2011), AJTEC2011-44629, 2011.
[80] S.M. Lee, K.Y. Kim, Optimization of zigzag flow channels of a printed circuit heat exchanger for nuclear power plant application, J. Nucl. Sci. Technol. 49 (3) (2012) 343–351.
[81] S.M. Lee, K.Y. Kim, A parametric study of the thermal-hydraulic performance of a zigzag printed circuit heat exchanger, Heat Transfer Eng. 35 (13) (2014) 1192–1200.
[82] S.M. Lee, K.Y. Kim, Multi-objective optimization of arc-shaped ribs in the channels of a printed circuit heat exchanger, Int. J. Therm. Sci. 94 (2015) 1–8.
[83] S.M. Lee, K.Y. Kim, Shape optimization of a printed-circuit heat exchanger to enhance thermal-hydraulic performance, ICAPP, Chicago, USA, 2012.
[84] S.M. Lee, K.Y. Kim, Comparative study on performance of a zigzag printed circuit heat exchanger with various channel shapes and configurations, Heat Mass Transf. 49 (7) (2013) 1021–1028.
[85] N. Bartel, M. Chen, V.P. Utgikar, et al., Comparative analysis of compact heat exchangers for application as the intermediate heat exchanger for advanced nuclear reactors, Ann. Nucl. Energy 81 (2015) 143–149.
[86] T. Ma, L. Li, X.Y. Xu, et al., Study on local thermal–hydraulic performance and optimization of zigzag-type printed circuit heat exchanger at high temperature, Energy Convers. Manage. 104 (2015) 55–66.
[87] H.H. Khan, A. Sharma, A. Srivastava, et al., Thermal-hydraulic characteristics and performance of 3D wavy channel based printed circuit heat exchanger, Appl. Therm. Eng. 87 (2015) 519–528.
[88] M. Chen, X. Sun, R.N. Christensen, et al., Pressure drop and heat transfer characteristics of a high-temperature printed circuit heat exchanger, Appl. Therm. Eng. 108 (2016) 1409–1417.
[89] S.G. Kim, Y. Lee, Y. Ahn, et al., CFD aided approach to design printed circuit heat exchangers for supercritical CO_2 Brayton cycle application, Ann. Nucl. Energy 92 (2016) 175–185.
[90] S.Y. Lee, B.G. Park, J.T. Chung, Numerical studies on thermal hydraulic performance of zigzag-type printed circuit heat exchanger with inserted straight channels, Appl. Therm. Eng. 123 (2017) 1434–1443.
[91] S.J. Yoon, J. O'Brien, M. Chen, et al., Development and validation of Nusselt number and friction factor correlations for laminar flow in semi-circular zigzag channel of printed circuit heat exchanger, Appl. Therm. Eng. 123 (2017) 1327–1344.
[92] N. Tsuzuki, Y. Kato, T. Ishiduka, High performance printed circuit heat exchanger, Bull. –Res. Laborat. Nucl. React. 29 (1/2) (2005) 141.
[93] N. Tsuzuki, Y. Kato, T. Ishiduka, High performance printed circuit heat exchanger, Appl. Therm. Eng. 27 (10) (2007) 1702–1707.
[94] T.L. Ngo, Y. Kato, K. Nikitin, et al., New printed circuit heat exchanger with S-shaped fins for hot water supplier, Exp. Therm Fluid Sci. 30 (8) (2006) 811–819.
[95] N. Tsuzuki, M. Utamura, T.L. Ngo, Nusselt number correlations for a microchannel heat exchanger hot water supplier with S-shaped fins, Appl. Therm. Eng. 29 (16) (2009) 3299–3308.
[96] N. Tsuzuki, Y. Kato, K. Nikitin, et al., Advanced microchannel heat exchanger with S-shaped fins, J. Nucl. Sci. Technol. 46 (5) (2009) 403–412.
[97] X. Zhang, X. Sun, R.N. Christensen et al. Optimization of S-shaped fin channels in a printed circuit heat exchanger for supercritical CO2 test loop. The 5th International Symposium–Supercritical CO2 Power Cycles, March 2016: 28-31.
[98] PROPATH Group. A program package for thermophysical properties of fluids, Version 10.2. Corona Publishing Co., Tokyo, Japan, 1990.
[99] T. Okinotani, N. Kawachi, K. Yamamoto, T. Ohara Research heat exchanger of natural refrigerant heat pump water heater. Proceedings of 2003 JSRAE Annual Conference.
[100] M. Utamura, K. Nikitin Full-scale CFD simulation of microchannel heat exchanger with S-shaped fins. The 19th International Symposium on Transport Phenomena, 17-20 August, 2008, Reykjavik, Iceland.
[101] M. Utamura, Thermal–hydraulic characteristics of microchannel heat exchanger and its application to solar gas turbine. Proc. ASME Turbo Expo 2007, Power for Land, Sea and Air, 14-17 May 2007, Canada.
[102] S.H. Yoon, H.C. No, G.B. Kang, Assessment of straight, zigzag, S-shape, and airfoil

PCHEs for intermediate heat exchangers of HTGRs and SFRs, Nucl. Eng. Des. 270 (2014) 334–343.
[103] X. Xu, T. Ma, L. Li, et al., Optimization of fin arrangement and channel configuration in an airfoil fin PCHE for supercritical CO_2 cycle, Appl. Therm. Eng. 70 (1) (2014) 867–875.
[104] X.Y. Xu, Q.W. Wang, L. Li, et al., Thermal-hydraulic performance of different discontinuous fins used in a printed circuit heat exchanger for supercritical CO_2, Numer. Heat Transf. Part A: Appl. 68 (10) (2015) 1067–1086.
[105] T. Ma, F. Xin, L. Li, et al., Effect of fin-endwall fillet on thermal-hydraulic performance of airfoil printed circuit heat exchanger, Appl. Therm. Eng. 89 (2015) 1087–1095.
[106] T.H. Kim, J.G. Kwon, S.H. Yoon, et al., Numerical analysis of air-foil shaped fin performance in printed circuit heat exchanger in a supercritical carbon dioxide power cycle, Nucl. Eng. Des. 288 (2015) 110–118.
[107] J.G. Kwon, T.H. Kim, H.S. Park, et al., Optimization of airfoil -type PCHE for the recuperator of small scale Brayton cycle by cost-based objective function, Nucl. Eng. Des. 298 (2016) 192–200.
[108] W. Chu, X. Li, T. Ma, et al., Study on hydraulic and thermal performance of printed circuit heat transfer surface with distributed airfoil fins, Appl. Therm. Eng. 114 (2017) 1309–1318.
[109] D. Fleming, J. Pasch, T. Conboy et al. Testing platform and commercialization plan for heat exchanging systems for SCO2 power cycles. ASME Turbo Expo 2013: Turbine Technical Conference and Exposition, Am. Soc. Mechan. Eng., 2013: V008T34A012.
[110] B. Rajabifar, S.K. Mohammadian, S.K. Khanna, Y. Zhang, Effects of pin tip-clearance on the performance of an enhanced microchannel heat sink with oblique fins and phase change material slurry, Int. J. Heat Mass Transf. 83 (2015) 136–145.
[111] B. Rajabifar, Enhancement of the performance of a double layered microchannel heatsink using PCM slurry and nanofluid coolants, Int. J. Heat Mass Transf. 88 (2015) 627–635.
[112] L. Chai, R. Shaukat, L. Wang, et al., A review on heat transfer and hydrodynamic characteristics of nano/microencapsulated phase change slurry (N/MPCS) in mini/microchannel heat sinks, Appl. Therm. Eng. 135 (2018) 334–349.
[113] J. Guo, Design analysis of supercritical carbon dioxide recuperator, Appl. Energy 164 (2016) 21–27.
[114] J. Guo, X. Huai, Performance analysis of printed circuit heat exchanger for supercritical carbon dioxide, J. Heat Transfer 139 (6) (2017) 061801.
[115] A. Bejan, Entropy generation through heat and fluid flow. Wiley, 1982.
[116] S. Kandlikar, S. Garimella, D. Li, S. Colin, M.R. King, Heat transfer and fluid flow in minichannels and microchannels, Elsevier, 2005.
[117] V. Singhal, D. Liu, S.V. Garimella, Analysis of pumping requirements for microchannel cooling systems, ASME 2003 International Electronic Packaging Technical Conference and Exhibition, Am. Soc. Mechan. Eng. (2003).
[118] S.V. Garimella, V. Singhal, Single-phase flow and heat transport and pumping considerations in microchannel heat sinks, Heat Transfer Eng. 25 (1) (2004) 15–25.
[119] L. Gosselin, A. Bejan, Tree networks for minimal pumping power, Int. J. Therm. Sci. 44 (1) (2005) 53–63.
[120] P. Canhoto, A.H. Reis, Optimization of forced convection heat sinks with pumping power requirements, Int. J. Heat Mass Transf. 54 (7–8) (2011) 1441–1447.
[121] T.H. Tsai, R. Chein, Simple model for predicting microchannel heat sink performance and optimization, Heat Mass Transf. 48 (5) (2012) 789–798.
[122] D. Liu, S.V. Garimella, Analysis and optimization of the thermal performance of microchannel heat sinks, ASME International Electronic Packaging Technical Conference and Exhibition, Am. Soc. Mechan. Eng. 2003 (2003) 557–565.
[123] P. Promvonge, S. Sripattanapipat, S. Kwankaomeng, Laminar periodic flow and heat transfer in square channel with 45° inline baffles on two opposite walls, Int. J. Therm. Sci. 49 (6) (2010) 963–975.
[124] G. Xia, L. Chai, M. Zhou, et al., Effects of structural parameters on fluid flow and heat transfer in a microchannel with aligned fan-shaped reentrant cavities, Int. J. Therm. Sci. 50 (3) (2011) 411–419.
[125] G. Xia, L. Chai, H. Wang, et al., Optimum thermal design of microchannel heat sink with triangular reentrant cavities, Appl. Therm. Eng. 31 (6) (2011) 1208–1219.
[126] L. Chai, G. Xia, M. Zhou, et al., Optimum thermal design of interrupted microchannel heat sink with rectangular ribs in the transverse microchambers, Appl. Therm. Eng. 51 (1) (2013) 880–889.
[127] L. Chai, G.D. Xia, H.S. Wang, Parametric study on thermal and hydraulic characteristics of laminar flow in microchannel heat sink with fan-shaped ribs on sidewalls-Part 3: Performance evaluation, Int. J. Heat Mass Transf. 97 (2016) 1091–1101.
[128] J. Zhang, Y. Zhao, Y. Diao, et al., An experimental study on fluid flow and heat transfer in a multiport minichannel flat tube with micro-fin structures, Int. J. Heat Mass Transf. 84 (2015) 511–520.
[129] R.L. Webb, Performance evaluation criteria for use of enhanced heat transfer surfaces in heat exchanger design, Int. J. Heat Mass Transf. 24 (4) (1981) 715–726.
[130] W.A. Khan, J.R. Culham, M.M. Yovanovich, Optimization of microchannel heat sinks using entropy generation minimization method, IEEE Trans. Compon. Packag. Technol. 32 (2) (2009) 243–251.
[131] M. Famouri, K. Hooman, F. Hooman, Effects of thermal boundary condition, fin size, spacing, tip clearance, and material on pressure drop, heat transfer, and entropy generation optimization for forced convection from a variable-height shrouded fin array, Heat Transfer Research 40 (3) (2009) 245–261.
[132] Z. Shi, T. Dong, Entropy generation and optimization of laminar convective heat transfer and fluid flow in a microchannel with staggered arrays of pin fin structure with tip clearance, Energy Convers. Manage. 94 (2015) 493–504.
[133] Y.L. Zhai, G.D. Xia, X.F. Liu, et al., Characteristics of entropy generation and heat transfer in double-layered micro heat sinks with complex structure, Energy Convers. Manage. 103 (2015) 477–486.
[134] G.N. Xie, B. Sundén, Q.W. Wang, Optimization of compact heat exchangers by a genetic algorithm, Appl. Therm. Eng. 28 (8) (2008) 895–906.
[135] M. Mishra, P.K. Das, S. Sarangi, Second law based optimization of crossflow plate-fin heat exchanger design using genetic algorithm, Appl. Therm. Eng. 29 (14) (2009) 2983–2989.
[136] D. Bacellar, V. Aute, Z. Huang et al. Novel Airside Heat Transfer Surface Designs Using an Integrated Multi-Scale Analysis with Topology and Shape Optimization. The 16th International Refrigeration and Air Conditioning Conference, July 11-14, 2016, Purdue, USA.
[137] K. Ogiso, Duality of heat exchanger performance in balanced counterflow systems, J. Heat Transfer 125 (3) (2003) 530–532.